

Abstract

In the field of cancer treatment, particle therapy has recently raised the interest of the community due to the high relative biological effectiveness of charged particles. In particular they prove to be more effective for targeting radio resistant or inoperable tumour. Nevertheless different sources of error can worsen the dose delivery profile, such as patient mis positioning, evolution of the tumour/morphology of the patient and imprecision in the treatment plannings, due to fragmentation of the incident beam and range uncertainties. As a consequence a three-dimensional non invasive imaging technique for ion beam therapy monitoring is required. The attention of the community is thus focused on positron emission tomography (PET).

In particular developments in the field of particle detectors push for the use of time of flight information, that allows to improve the sensitivity by improving the signal to noise ratio (SNR). In order to benefit from a significative reduction of the SNR, the target is less than 100 ps FWHM coincidence time resolution for the two detectors. The standard solution for future PET scanners is to make use of heavy scintillating crystals coupled to Silicon PhotoMultipliers.

This thesis is devoted to the full characterization of the parameters that influence time resolution in a scintillator/photodetector setup, with particular attention focused on the impact of time profiles of heavy scintillators on the performance.

The first part of the presented work has the objective of describing the fundamental model that governs light production and collection in a PET-like setup. To

this purpose a model based on multi-exponential time profiles has been implemented on an existing framework, widening the scope of usage by evaluating the role of Cerenkov photons produced by low energy radiation.

Moreover in order to properly characterized the operational parameters of a scintillator setup, a comparative analysis of ray tracing softwares has been conducted, namely two packages SLitrani and Geant4. The latter has been chosen to build the simulation framework that allowed to disentangle the various source of resolution degradation.

Finally the work focused on the measurements and evaluation of rise time. Non zero rise time in scintillating systems is given by the different processes characterizing energy deposition inside a crystalline lattice, with utmost relevance of the latest stage of electron hole thermalization. The time scale of this phenomenon is ~ 100 ps and until now has proven to be difficult to estimate due to the intrinsic limitations of detection setups. Samples of different crystalline species such as CeF_3 , LSO:Ce , LuAG:Ce , LuAG:Pr with different doping concentration are the subject of a time resolved analysis. Data taking has been performed in two different conditions: excitation at low energy (36 eV) and a PET-like setup (511 KeV).

The first set of measurements has been performed at the VUV beamline at Celia, Bordeaux, with an excitation energy of 36 eV. The data show results broadly separable in to two main groups: crystals in the LuAG group, with rise times > 100 ps, and crystals belonging to the LSO group with rise times < 50 ps. This is due to the different energy transfer mechanism.

The samples were then measured with a positron source (Na^{22}) on a experimental bench composed by a MCP-PMT stop detector and a tagging crystal readout by an amplified SiPM. Rise time order of magnitude proved to be accessible, though maintaining large uncertainties due to the limited resolution and the long accumulation times. Nonetheless we showed that Cerenkov photons and deep volume excitations

introduce a non negligible contribution to the measured rise time. In particular the samples, excited above the Cerenkov threshold and in the deep volume of the crystal due to the energy of the excitation, showed slower rise times, above 100 ps. Moreover the influence of Teflon diffusive wrapping have been investigated, showing that opening the extraction cone of the crystals leads to higher rise times due to coupling of multiple reflection modes.

Contents

Abstract	i
List of Figures	ix
1 Motivations	1
1.1 Particle therapy	3
1.1.1 Ion beam therapy	3
1.1.2 Beam delivery	4
1.1.3 Monitoring of the beam	6
1.2 Positron Emission Tomography	7
1.2.1 Principles	7
1.2.2 Image reconstruction	9
1.2.3 Sources of noise and sensitivity	10
1.2.4 Time-Of-Flight PET	12
1.3 Outline of the thesis	14
1.3.1 From high energy physics to medical applications	14
1.3.2 Study of time profiles	15
2 Scintillating detectors	17
2.1 Introduction to particle detectors	17
2.2 Interaction of radiation with matter	17
2.2.1 Photoelectric effect	18

2.2.2	Compton scattering	19
2.2.3	Pair production	20
2.3	The scintillation mechanism	21
2.3.1	Creation of electron hole pairs	22
2.3.2	Intrinsic luminescence	24
2.3.3	Core to valence transitions	25
2.3.4	Extrinsic luminescence	25
2.3.5	Quenching phenomena	26
2.4	Operational parameters	26
2.4.1	Light yield	26
2.4.2	Optical properties and light transport	27
2.4.3	Rayleigh scattering	27
2.4.4	Energy resolution and nonproportionality	27
2.4.5	Cerenkov effect	29
2.5	Scintillators in PET detectors	31
3	Photo detectors	32
3.1	Photo multiplier tubes	33
3.1.1	Properties of PMT	34
3.2	Micro Channel Plate-PMT	35
3.2.1	Properties of MCP	36
3.3	Silicon photo multipliers	38
3.3.1	Analog SiPM	39
3.3.2	Properties of SiPM	40
3.3.3	The NINO chip	42

4	A model for scintillation counting	44
4.1	Signal formation	44
4.1.1	Scintillation pulse	44
4.1.2	Cerenkov pulse	45
4.2	The Cramer-Rao lower bound	45
4.3	The order statistics	46
4.4	Intrinsic time resolution	47
4.5	Effects on signal extraction	47
5	MonteCarlo simulation tools	48
5.1	Ray tracing	48
5.2	Geant4	48
5.2.1	Physics	48
5.2.2	Implementation	48
5.3	SLitrani	48
5.3.1	Physics	48
5.3.2	Implementation	48
5.4	A comparison for timing simulation	48
5.5	Simulation input parameters	48
5.5.1	Light yield	48
5.5.2	Optical transmission	51
5.5.3	Fluorescence spectrum	51
6	Methods	52
6.1	Time Correlated Single Photon counting	52
6.1.1	Excitation	52
6.1.2	Detection	52

6.2	Data analysis techniques	52
6.2.1	Iterative reconvolution	52
6.2.2	Error estimation	54
6.3	Simulations	54
7	Na-22 measurement	55
7.1	Phenomenology	55
7.2	Experimental setup	55
7.3	Preliminaries	56
7.3.1	Characteristics of the start signal	56
7.3.2	Characteristics of the stop signal	56
7.3.3	IRF measurements	56
7.3.4	Control of the bias fraction	56
7.4	Data analysis	56
7.4.1	Cuts	56
7.4.2	Fit procedure	56
7.4.3	Results	56
8	VUV measurement	57
8.1	High Harmonic Generation	57
8.2	Experimental setup	58
8.2.1	Laser beamline	59
8.2.2	VUV line	59
8.2.3	Detection system	61
8.3	Preliminaries	62
8.3.1	VUV spectrum	62
8.3.2	IRF measurement	62

8.3.3	Control of the bias fraction	62
8.4	Data analysis	62
8.5	Fit procedure	62
8.6	Results	62
9	Conclusions	63
	Bibliography	64

List of Figures

1.1	X-ray and proton irradiation	2
1.2	Depth dose comparison	3
1.3	RBE comparison	4
1.4	Peak spread for Carbon	6
1.5	PET scanner	8
1.6	Image reconstruction in PET	9
1.7	Coincidencies in PET exam	11
1.8	TOF-PET schematics	13
1.9	Improvement of TOF-PET	14
2.1	Photo electric effect	19
2.2	Compton scattering	20
2.3	γ cross section	21
2.4	Energy deposition in scintillator	22
2.5	Electron hole recombination	24
2.6	Core to valence luminescence	25
2.7	Cerenkov effect	30
2.8	Cerenkov emission cone	31
3.1	PMT schematics	33
3.2	MCP principle	36
3.3	MCP schematics	36

3.4	I-V plot Silicon detectors	38
3.5	Example of SiPM	39
3.6	SiPM layer structure	40
3.7	NINO chip	42
3.8	Time-over-threshold	43
7.1	Na ²² decay scheme	56
8.1	HHG phenomenology	58
8.2	VUV line	59
8.3	VUV spectrum	60
8.4	VUV DAQ	62

1

Motivations

Cancer is considered to be the second biggest killer after cardiovascular diseases: there were an estimated 14.1 million cancer cases around the world in 2012, of these 7.4 million cases were in men and 6.7 million in women. This number is expected to increase to 24 million by 2035(9).

Although surgery remains the most diffuse and successive treatment, radiotherapy is an important and effective option used for curative and palliative management of malignant tumors. In approximately the 50% of clinical cases, radiation therapy is a part of the initial treatment and it is usually conducted by means of high-energy X-rays(7).

Results of radiotherapy are improved when a high dose of radiation with high biological effectiveness is delivered to the tumour with the least possible dose to the surrounding tissues, especially in the case of critical organs(17). In order to increase the conformity of the dose delivered to the tumour, diverse technologies have been considered and used. Traditional forms of radiotherapy, X-ray tubes (energy ~ 100 keV) or radioactive isotopes, have been replaced by linear accelerator delivering (~ 10 MeV) from different directions (e.g. Intensity Modulated Radio Therapy).

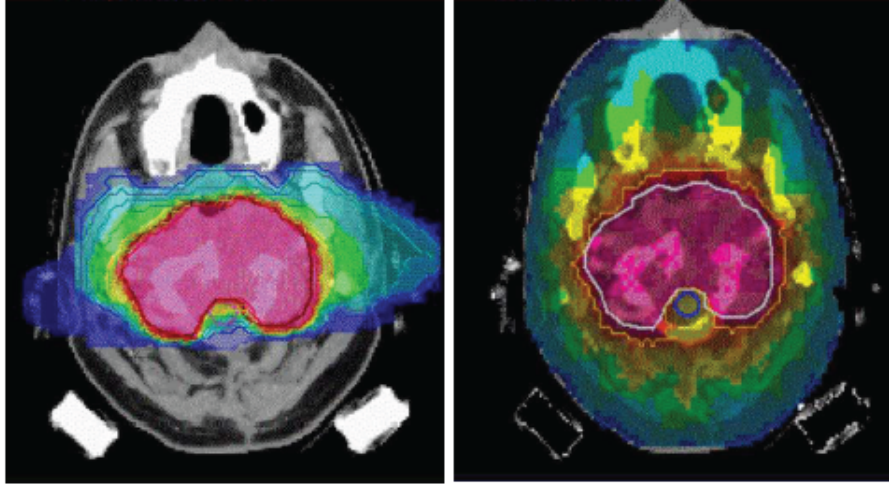


FIGURE 1.1: Comparison of treatment plans for a large target volume in the base of the skull. Plan for carbon ions (left) and IMRT (right)(7).

Although being widely used as a standard in radiation therapy, the effectiveness of conventional electromagnetic radiation is limited by the intrinsic characteristics of interaction with matter. In particular two aspects disfavours the usability of electromagnetic radiation with respect to ion for tumour targeting: the depth dose profile, which does not allow for an optimal dose deposition to the tumour sparing vital organs, and the inferior biological effectiveness, which is the limiting factor in case of radio resistant tumours. Heavier charged particles, like protons and ions (He-Ca) have the potentiality to overcome the limits of conventional therapy. With respect to this, the scientific community is directing his attention towards possible improvements of ion beam therapy(1).

The work outlined in these pages have been sponsored by *The European training network in digital medical imaging for radiotherapy* (ENTERVISION) at the *European Center of Nuclear Research* (CERN). ENTERVISION was established in February 2011 in response to the critical need for reinforcing research in online 3D digital imaging in order to deliver some of the key elements and building blocks for realizing the vision for early detection and more precise treatment of tumours.

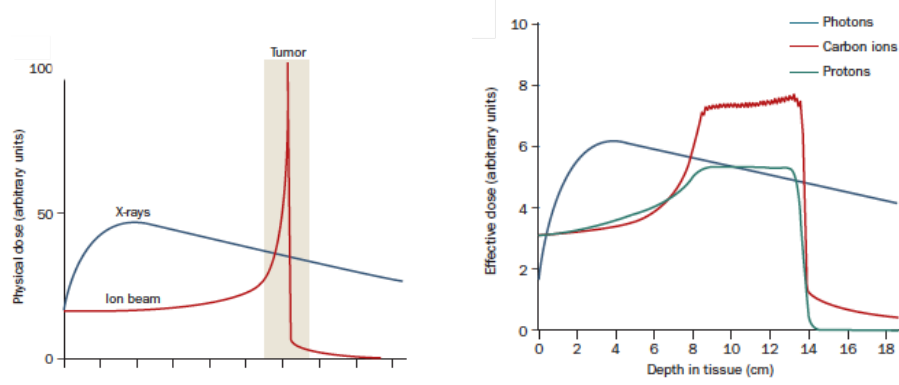


FIGURE 1.2: Comparison of the depth-dose relationships for X-rays and high-energy charged particles. In treatment of large tumors, the Bragg peak must be broadened by use of overlapping beams with different energies(7).

1.1 Particle therapy

1.1.1 Ion beam therapy

The first proposition of ion beam therapy was presented in 1946 by R. Wilson(26). The original idea was to exploit the physical properties of ion interaction in matter to improve the precision in radiotherapy treatments. Making use of the so called Bragg peak, that is using the fact that protons and ions in general deposit a maximum of energy at the end of their trajectory, the treatment could save the surrounding tissue from radiation overdose.

The dose deposited by photons, considered as the gold standard for tumour treatment, is maximum close to the beginning of the trajectory in the body and is characterized by an exponential decrease. As a consequence an undesired radiation dose is delivered to healthy tissues around the targeted tumour.

The recent therapeutic interest of ions in the field of radiotherapy relies mainly on their high relative biological effectiveness. LET (linear energy transfer) has long been viewed as the main parameter to discern the biological effect of different kinds of radiation. It is a measure for the energy deposited by a charged particle traveling through matter. LET is closely related to stopping power and is not a constant

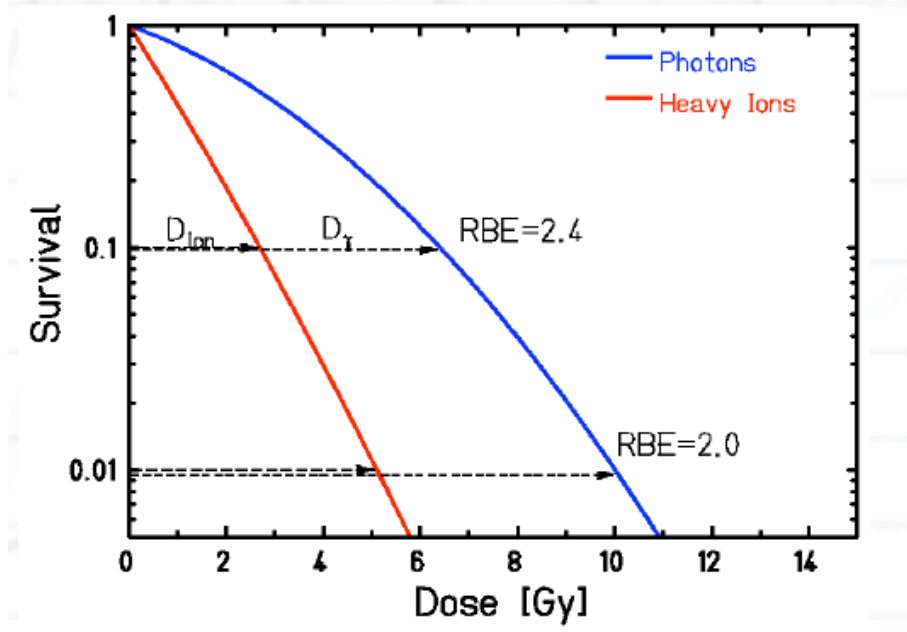


FIGURE 1.3: Comparative plot of RBE for photons and heavy ions.

value, since it changes along the particle's path (es 10 KvV/ μm for photons, 100 KeV/ μm for protons, 1000 KeV/ μm for ions). When considering ions of different atomic number LET becomes a limited parameter to evaluate the biological effect.

In this sense the relative biological effectiveness (RBE) is considered the most accurate quantity, since it is defined as the biological effect of one type of ionizing radiation relative to another, given the same amount of absorbed energy. As the charge of the incident ions increases, so does the probability of severe DNA damage. An elevate RBE in the Bragg peak region has clearly been demonstrated for ions heavier than Helium (17). As a consequence they prove to be more effective for targeting radio resistant or inoperable tumours.

1.1.2 Beam delivery

Ion beams are delivered by either cyclotrons or synchrotrons. In the first case the beam has a fixed energy which is tuned by means of degraders in order to deliver the correct dose profile. In the case of synchrotron the beam is delivered in spills and

the energy is varied between spills. In the case of Carbon only synchrotrons can be used. To deliver the dose to the planned target volume (PTV) different energies are superimposed in order to obtain the so-called spread-out Bragg peak (SOBP). The beam is usually delivered in a passive beam shaping setup or a scanning system.

Different sources of error can worsen the dose delivery profile, such as patient mis positioning and evolution of the tumour/morphology of the patient. In addition the complex physics of ion interaction leads to imprecision in the treatment plannings, due to fragmentation of the incident beam and range uncertainties.

Usually treatment planning systems cope with these problems by irradiating a volume larger than the tumour itself, called planning target volume (PTV) which contains the clinical target volume (CTV). Complex compensating systems, including x-ray imaging techniques and patient positioning systems, allow to reduce errors in the dose profiles delivered. Treatment plannings of ion therapy rely for example on accurate values of particle range in tissue obtained from Hounsfield unit of computed tomograms, leading to uncertainties of 1 – 3% in range calculations(8).

The dose delivered by a ion beam system is much more sensitive to these deviations than the one delivered by a photon beam. Due to the high biological effectiveness of ion beams wrong ranges could lead to dramatic under dosage to the tumour or over dosage to organ at risk surrounding. As a consequence a three-dimensional non invasive imaging technique for ion beam therapy monitoring is required. Since ions, unlike photons, are stopped completely in the patient volume, technology like portal imaging are not suitable. The attention of the community is thus focused on positron emission tomography (PET), which relies on the peculiar characteristics of β^+ decay.

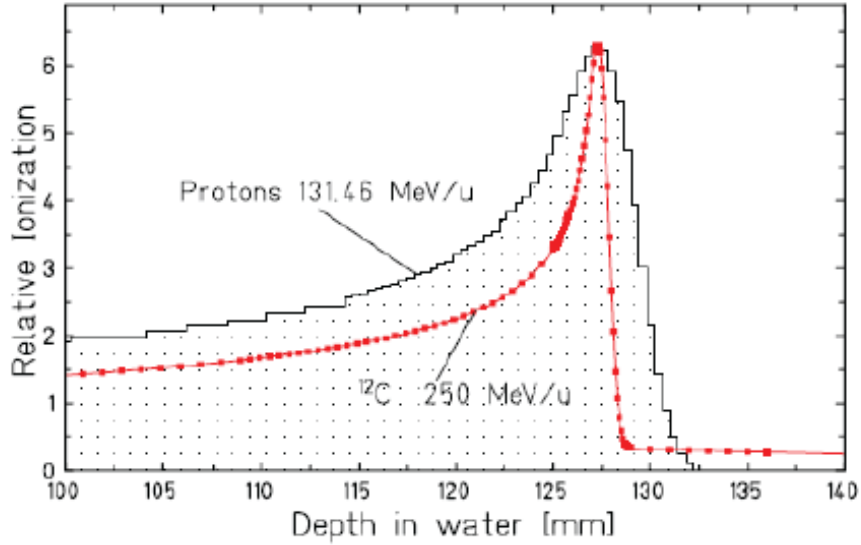


FIGURE 1.4: Bragg curves of proton and C-ions having the same mean range (water phantom and ionization chamber) (21).

1.1.3 Monitoring of the beam

Several attempts have already been undertaken to systematically assess the benefit of the PET method for beam monitoring, the principal one being the set up installed at the experimental carbon ion therapy unit at the Gesellschaft für Schwerionenforschung Darmstadt (GSI)(19). Two alternatives can be considered: the use of positron radioactive ions as projectiles for dose delivery or the detection of β^+ activity given by nuclei fragmentation. As an example of the first approach it is interesting to consider the effort made at the Heavy Ion Accelerator in Chiba (Japan), where radioactive beams of $^{11}\text{C} - ^{10}\text{C}$ ions deliver an activity of $10^3 - 10^5 \text{ Bq Gy}^{-1} \text{ cm}^{-3}$ within the irradiated volume. Due to the low production rate of secondary radioactive ions, this approach has been only partially successful.

Another possibility is to make use of the β^+ activation given by the fragmentation of stable ions interacting with the tissue. The radioactivity is a direct product of the irradiation and, although the activity density is rather low (around 600

$Bq\ Gy^{-1}\ cm^{-3}$ for protons), this method provides a rather cheaper and feasible solution(8). The activity slides very fast under a reasonable threshold for detectability and the most effective solution is an in-beam scanner. In-beam PET is currently the main method implemented clinically for in situ monitoring of charged hadron radiotherapy(5).

1.2 Positron Emission Tomography

1.2.1 Principles

Positron Emission Tomography (PET) has been introduced as a nuclear medicine imaging technique which measures the distribution of a positron-emitting radionuclide (tracer), which is injected into the body on a biologically active molecule. In the case of in-beam PET the activity is present in the body of the patient due to the activation induced by proton interaction.

After the injection, or during the dose delivery, the subject of a PET study is placed within the field of view (FOV) of a number of detectors capable of registering incident gamma rays. The radionuclide in the radio tracer decays and the resulting positrons subsequently annihilate with electrons after travelling a short distance ($\sim 1\ mm$) within the body.

Each annihilation produces two 511 keV photons travelling in opposite directions and these photons may be detected by the detectors surrounding the subject. The detector electronics are linked so that two detection events unambiguously occurring within a certain time window may be called coincident and thus be determined to have come from the same annihilation. These "coincidence events" can be stored in arrays corresponding to projections through the patient and reconstructed using standard tomographic techniques. The resulting images show the tracer distribution throughout the body of the subject. The scheme of a PET scanner is shown in figure ??.

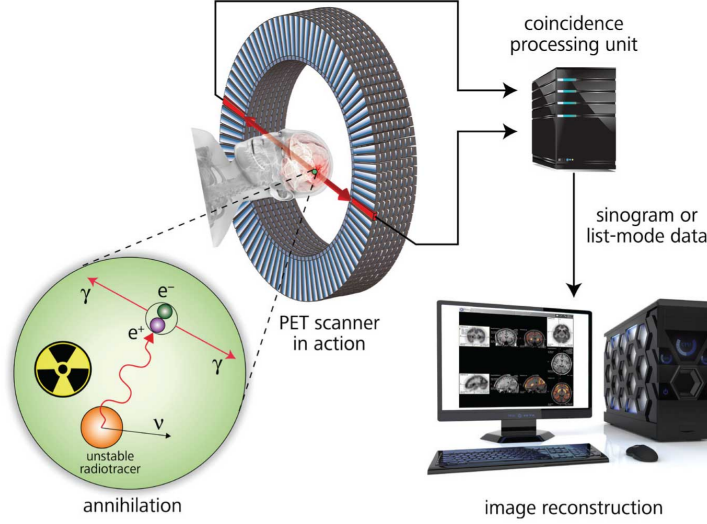


FIGURE 1.5: Schematic view of PET scanner.

Positron emission tomography relies on the β^+ decay of a radionuclide. The nucleus of the radionuclide can convert a proton into a neutron

$$p \rightarrow n + e^+ + \nu_e$$

As positrons travel through human tissue, they give up their kinetic energy principally by Coulomb interactions with electrons. As the rest mass of the positron is the same as that of the electron, the positrons may undergo large deviations in direction with each Coulomb interaction, and they follow a tortuous path through the tissue as they give up their kinetic energy.

When the positrons reach thermal energies, they start to interact with electrons either by annihilation, which produces two 511 keV anti-parallel photons, or by the formation of a hydrogen-like orbiting couple called positronium. In its ground-state, positronium has two forms: ortho-positronium, where the spins of the electron and positron are parallel, and para-positronium, where the spins are anti-parallel. Para-positronium again decays by self-annihilation, generating two anti-parallel 511 keV photons. Ortho-positronium self-annihilates by the emission of three photons. Both forms are susceptible to the pick-off process, where the positron annihilates with

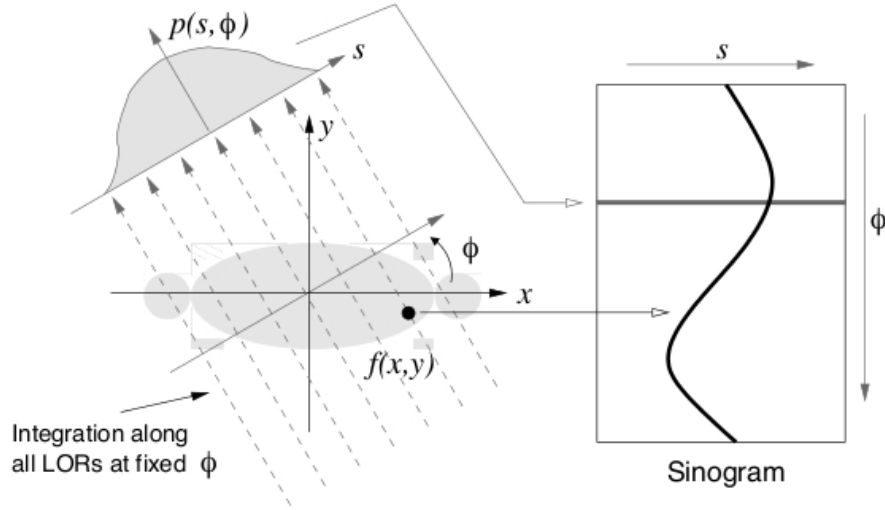


FIGURE 1.6: Extraction of a sinogram from a 2D acquisition.

another electron. Free annihilation and the pick-off process are responsible for over 80% of the decay events.

1.2.2 Image reconstruction

After all corrections have been applied to the data acquired, the number of counts assigned to a LOR joining a pair of crystals is proportional to a line integral of the activity along that LOR. Parallel sets of such line integrals are known as projections. For image reconstruction, the most commonly used algorithms are the analytical method called filtered back projection and iterative reconstruction schemes. In particular iterative methods are often preferred over analytical approaches because they can account more effectively for the noise structure and can use a more realistic model of the system. Moreover advances in computation speed and faster algorithms allowed iterative methods to receive growing clinical acceptance. An iterative method has five basic components.

- A model for the image, that is a discretization of the image domain into pixels (2-D) or voxels (3-D) or other exotic models.

- A system model that relates the image to the data. A system model M is characterized by elements M_{ij} related to the image system that represent the probability that an emission from voxel j is detected in projection i
- A model for the data which describes the statistical relation between the value obtained and the value expected
- A governing principle that defines the parameters of a "best" image, often expressed as a cost function (e.g. Maximum likelihood)
- An algorithm that optimizes the cost function.

This last issue has been implemented in several ways, ranging from gradient-based algorithms to the commonly used EM algorithm and its variations (OSEM).

1.2.3 Sources of noise and sensitivity

In a PET scanner, each detector generates a timed pulse when it registers an incident photon. These pulses are then combined in coincidence circuitry, and if the pulses fall within a short time-window, they are deemed to be coincident. A coincidence event is assigned to a line of response (LOR) joining the two relevant detectors. In this way, positional information is gained from the detected radiation without the need of a physical collimator. This is known as electronic collimation. When a physical collimator is used, directional information is gained by preventing photons which are not normal or nearly normal to the collimator face from falling on the detector. In electronic collimation, these photons may be detected and used as signal. Coincidence events in PET fall into four categories: true, scattered, random and multiple, as shown in figure .

True coincidences occur when both photons from an annihilation event are detected by detectors in coincidence, neither photon undergoes any form of interaction prior to detection, and no other event is detected within the coincidence time-window.

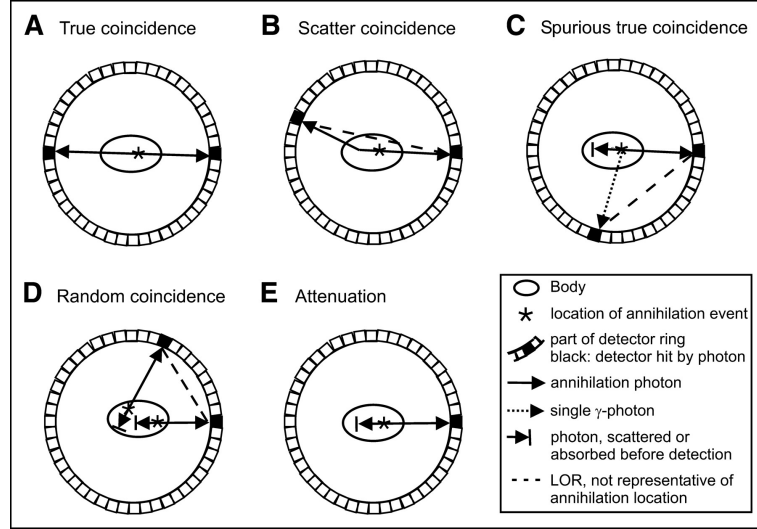


FIGURE 1.7: Phenomenology of PET examination. The cases b, c, d lead to loss of resolution.

A scattered coincidence is one in which at least one of the detected photons has undergone at least one Compton scattering event prior to detection. Since the direction of the photon is changed during the Compton scattering process, it is highly likely that the resulting coincidence event will be assigned to a wrong LOR. Scattered coincidences add background to the true coincidence distribution which changes slowly with position, decreasing contrast and causing the isotope concentrations to be overestimated. They also add statistical noise to the signal. The number of scattered events detected depends on the volume and attenuation characteristics of the object being imaged, and on the geometry of the PET scanner.

Random coincidences occur when two photons not arising from the same annihilation event are incident on the detectors within the coincidence time window of the system. The number of random coincidences in a given LOR is closely linked to the rate of single events measured by the detectors joined by that LOR and the rate of random coincidences increase roughly with the square of the activity in the FOV. As with scattered events, the number of random coincidences detected also depends on the volume and attenuation characteristics of the object being imaged, and on the

geometry of the scanner. The distribution of random coincidences is fairly uniform across the FOV, and will cause isotope concentrations to be overestimated if not corrected for. Random coincidences also add statistical noise to the data.

1.2.4 *Time-Of-Flight PET*

It has been shown that in-beam PET could not provide definitive information to the oncologist when medium to large tumors are involved(10). This is due to the operative parameters of scanners available on the market, with relatively slow scintillators and tomographs covering small solid angles. A decisive improvement could be given by time-of-flight PET (TOF-PET).

Recent developments in scintillator technology and read out electronics allow to build detectors able to detect the time difference between the moment of detection of the opposed gamma rays in coincidence.

If we define a LOR between two detectors A and B, the distance between the center of the LOR and the annihilation point is given by

$$x = (t_b t_a) \cdot c/2 \tag{1.1}$$

where c is the speed of light. Thus the spatial resolution is proportional to the coincidence time resolution (CTR) of the system. Scanners available on the market today could deliver a 600 picoseconds time resolution, that translates to a positional uncertainties of 9 cm (FWHM) on the LOR. The quality of the tomographic image largely benefits from the timing information of a TOFPET scanner, since it reduces considerably the contribution of Compton scattered photons and from photons from outside the field-of-view (FOV). As a consequence the background from scattered and random coincidence is largely suppressed.

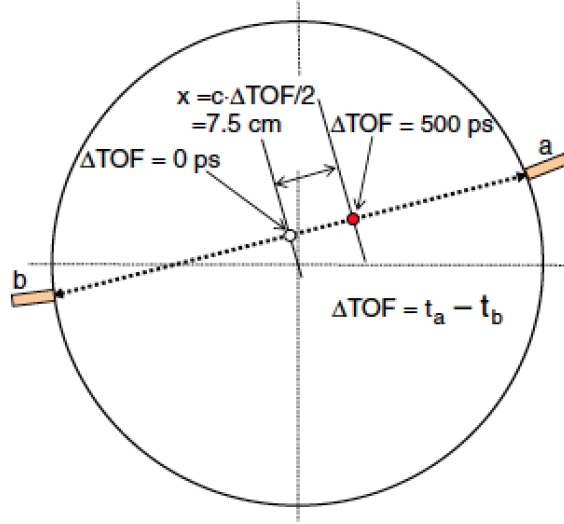


FIGURE 1.8: Example of time of flight information usage in PET examination.

The signal to noise ration (SNR) is thus dramatically improved(14). In the case of in-beam PET this is relevant, since it has been shown (Fiedler et al 2007) that during particle irradiation an considerable amount of activity is transported outside the FOV by metabolic processes. Moreover a high background signal is typical of carbon ion beams (8). A useful and pratical estimation of the gain in signal to noise can be formalized as follows

$$G = \frac{SNR_{TOF}}{SNR_{nonTOF}} = \sqrt{\frac{2 \cdot D}{c \cdot CTR}}$$

where D is the diameter of the volume under examination, c is the speed of light and CTR is the coincidence time resolution. Thus a CTR of 100 ps FWHM translates into a 1.5 cm resolution on the position and a SNR gain of 5 (corresponing to a sensitivity gain of about a factor 25) compared to non TOF systems.

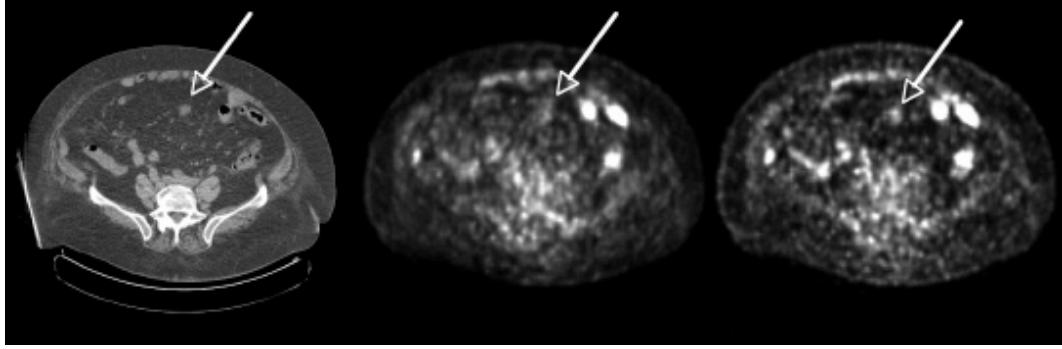


FIGURE 1.9: Representative transverse sections: low dose CT (left), non-TOF ML-EM (middle), and TOF ML-EM (right). The patient with colon cancer (119 kg, BMI = 46.5) shows a lesion in the abdomen seen in CT much more clearly in the TOF image than in the non-TOF image.(14)

1.3 Outline of the thesis

1.3.1 *From high energy physics to medical applications*

The present work was hosted by CERN, the European Organisation of Nuclear Research, based in Geneva, Switzerland. CERN was established by a formal act in Paris, on 1st of July 1953, as an organisation that shall provide for collaboration among European States in nuclear research of a pure scientific and fundamental character, and in research essentially related thereto. Throughout its history, CERN provided experimental and theoretical tools to study and understand the fundamental forces governing our universe, in a continuous effort to improve our understanding of elementary physics.

The ECAL detector at the CMS experiment at the LHC was built with the fundamental contribution of the collaboration hosting this thesis: the Crystal Clear Collaboration. It was founded in 1990 as an international academic network of laboratories and industrial partners for the development of scintillating crystal detectors as well as their applications. It comprises experts in crystallography and solid state physics as well as in radiation detection and instrumentation. Its first goal was the development of a radiation-hard crystal for the ECAL detector, leading to the de-

velopment of PbWO₄ (PWO) as the material selected for CMS calorimeter. More recently the group has been focusing on the study of new materials for hadronic and electromagnetic calorimeters for future particle accelerators. In parallel, the collaboration engaged in a effort of technology transfer to other domains exploiting the expertise developed in scintillating detectors. It is quite natural to focus the attention to medical physics, with particular respect to nuclear medicine since the requirements for detectors used in medical physics and detectors for high energy experiments are similar.

1.3.2 Study of time profiles

This thesis is devoted to the full characterization of the parameters that influence time resolution in a scintillator/photodetector setup, with particular attention focused on the impact of time profiles of heavy scintillators on the performance.

The first part of the presented work has the objective of describing the fundamental model that governs light production and collection in a PET-like setup. To this purpose a model based on multi-exponential time profiles has been implemented on an existing framework, widening the scope of usage by evaluating the role of Cerenkov photons produced by low energy radiation.

Moreover in order to properly characterized the operational parameters of a scintillator setup, a comparative analysis of ray tracing softwares has been conducted, namely two packages SLitrani and Geant4. The latter has been chosen to build the simulation framework that allowed to disentangle the various source of resolution degradation.

Finally the work focused on the measurements and evaluation of rise time. Non zero rise time in scintillating systems is given by the different processes characterizing energy deposition inside a crystalline lattice, with utmost relevance of the latest stage of electron hole thermalization. The time scale of this phenomenon is ~ 100 ps and

until now has proven to be difficult to estimate due to the intrinsic limitations of detection setups.

Thus a time resolved study of different species of crystals is proposed in the last two chapters of this thesis. Namely the excitation is varied from the 36 eV of a VUV femtosecond source to the 511 KeV of a γ source.

2

Scintillating detectors

2.1 Introduction to particle detectors

In the field of medical applications, the energies of the gamma photons to be detected are usually of the order of hundreds of keV. In the case of PET scanners the energy of the two back to back photons is 511 keV. A simple approach to estimate the parameters of the incoming radiation is to make use of a fluorescent sample coupled to a photodetector. A standard set up would include a heavy scintillator crystal which converts the incoming radiation into visible photons. The following steps of the detection process involve transportation to the entrance window of the photodetector, conversion of the photons into an electric signal and subsequent manipulation of the signal by readout electronics.

2.2 Interaction of radiation with matter

In this work we are mainly concerned with the interaction of gamma radiation with matter, thus focusing our attention on the three existing mechanisms: photo electric interaction, Compton interaction and pair production. A brief description of

Rayleigh scattering will be given, as a non-ionizing type of scattering. Moreover electrons produced by ionizing interactions can polarize the medium, giving origin to the Cerenkov effect and producing visible photons, which can be of foremost importance in the case of timing application.

2.2.1 Photoelectric effect

In the case of the photoelectric effect an electron from an atom is freed upon absorption of the incoming photon:

$$\gamma + atom \rightarrow e^- + atom \quad (2.1)$$

Due to conservation of momentum and energy this phenomenon does not occur with free electrons. The gamma energy transferred to the electron equals the binding energy of the electron itself minus its resulting kinetic energy E_{e-}

$$E_{e-} = E_{\gamma} - E_b \quad (2.2)$$

The photoelectric effect is predominant at low energies ($E \leq 100keV$) and favours tightly bound K-shell electrons. An approximation of the photo electric cross section is given by

$$\sigma_{pe} \propto \frac{Zn}{E_{\gamma}^{3.5}} \quad (2.3)$$

The vacancy created can be filled through capture of bound or free electrons, eventually generating characteristics X-rays.

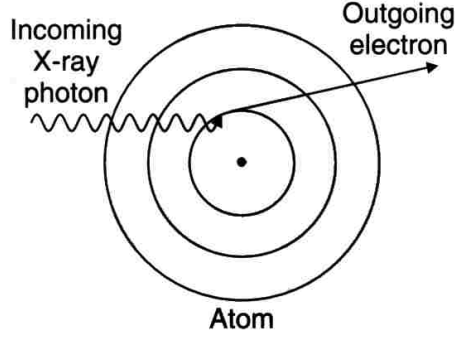


FIGURE 2.1: Phenomenology of photo electric effect

2.2.2 Compton scattering

Compton scattering is the inelastic scattering of the incoming photon with a weakly bound electron in the material.

$$\gamma + atom \rightarrow (\gamma') + e^- + atom^* \quad (2.4)$$

Contrary to the photoelectric effect, this only concerns quasi-free electrons of the material. The photon transfers part of its energy to the electron, which is freed from its shell. Applying conservation of energy and momentum it is possible to derive the energy of the scattered gamma as well as the direction and energy of free electron.

$$E_{\gamma'} = \frac{E_{\gamma}}{1 + \frac{E_{\gamma}}{m_e c^2} (1 - \cos\theta)} \quad (2.5)$$

The angular distribution can be described by the Klein-Nishina formula. It is evident from the plot that forward scattering direction are favoured as the incoming photon energy increases

$$\frac{d\sigma_{cpt}}{d\omega} = Z \cdot \frac{e^2}{4\pi\epsilon_0 m_e c^2} \cdot \frac{1}{2} \cdot \frac{E'_{\gamma}}{E_{\gamma}} \left(1 - \frac{E'_{\gamma}}{E_{\gamma}} \cdot \sin^2\theta + \left[\frac{E'_{\gamma}}{E_{\gamma}} \right]^2 \right) \quad (2.6)$$

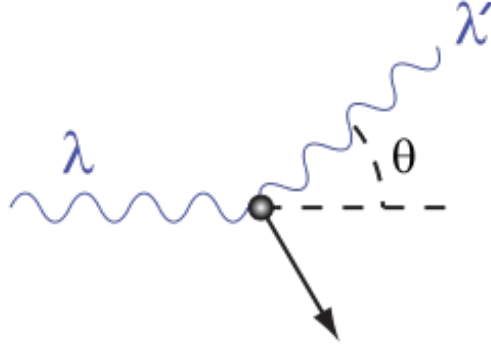


FIGURE 2.2: Phenomenology of Compton scattering

The total cross section can be computed by integrating the differential cross section over the angle, with $\epsilon = h\nu/mc^2$ and $r_e = h/mc$.

$$\sigma_{KN} = 2\pi r_e^2 \frac{1+\epsilon}{\epsilon^2} \left[\frac{2(1+\epsilon)}{1+2\epsilon} - \frac{\ln(1+2\epsilon)}{\epsilon} \right] + \frac{\ln(1+2\epsilon)}{2\epsilon} - \frac{1+3\epsilon}{(1+2\epsilon)^2} \quad (2.7)$$

2.2.3 Pair production

If the energy of the gamma exceeds $2m_e c^2 = 1.02$ MeV, the impinging photons can also be converted into an electron-positron pair. The cross-section of the pair production is given at low energies (thus low screening) by

$$\sigma_{pair} = 4\alpha r_e^2 Z^2 \left(\frac{7}{9} \ln 2 \frac{E}{m_e c^2} - \frac{109}{54} \right) \quad (2.8)$$

The cross section is very low compared to that of photoelectric and Compton effect until the energy of the gamma approaches several electron Volts. Thus for the energies involved in medical applications pair production can be neglected.

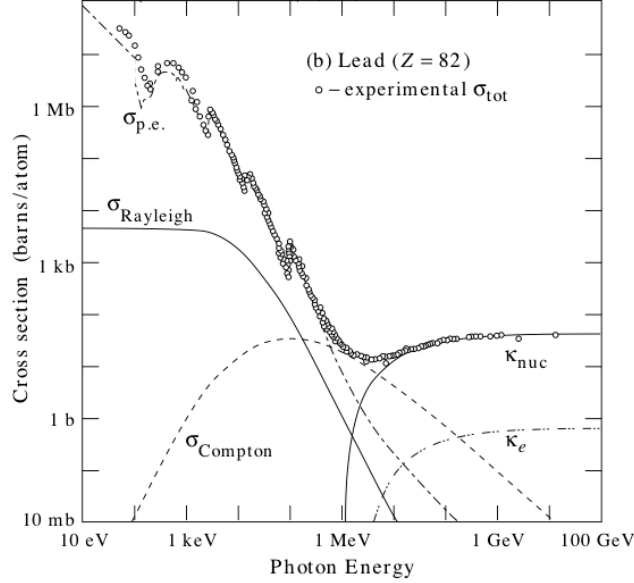


FIGURE 2.3: Cross section for the different processes in lead

2.3 The scintillation mechanism

As a general idea the scintillation process can be considered as the conversion of the energy of an incident gamma quantum or particle into a certain number of low energy photons(20). In a way it can be therefore defined as a wavelength shifting process(16).

After a ionization event, generated by the mechanisms presented above in the case of a gamma interaction, the scintillator relaxes towards a new equilibrium. This process is characterized by a multitude of sub processes, that can be depicted by band diagrams as the one in figure As long as the energy of the particles is high enough, it is transferred to secondary particles of low energy, creating an electromagnetic cascade. A crystal though is an ordered ensemble of atoms, so the electrons in the KeV range start to couple with electrons and atoms of the lattice. As a result of their interaction with electronic states of the material, couples of electrons and relative vacancies are created. The electron hole pairs migrate in the lattice above and below the ionization threshold until they are trapped by a defect or recombine on a luminescent center.

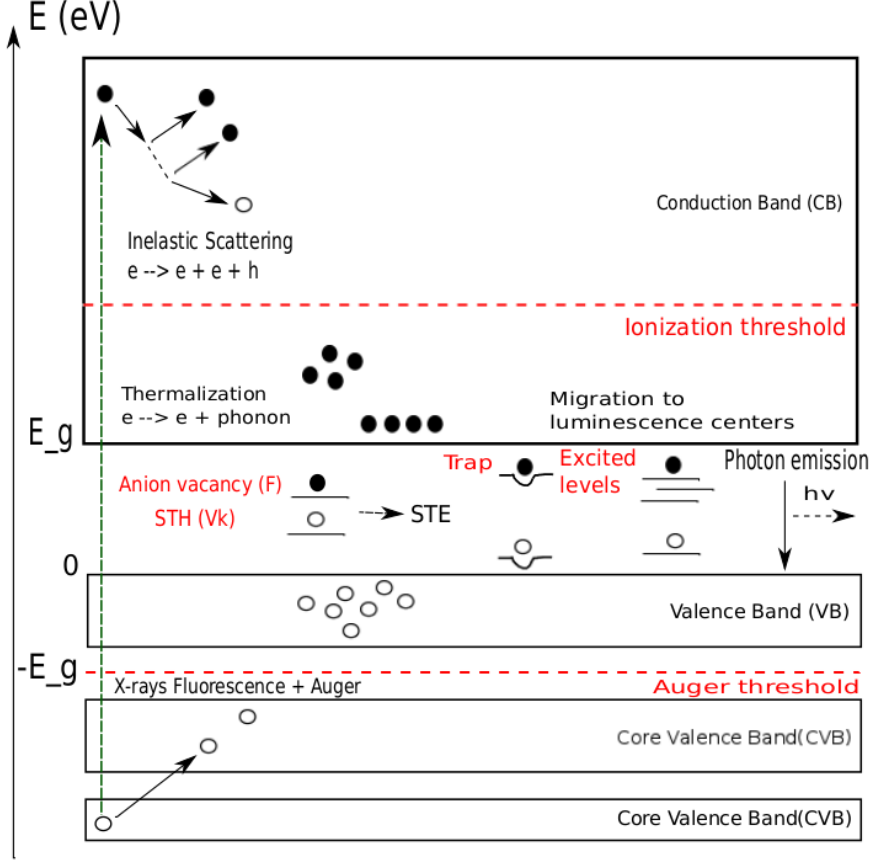


FIGURE 2.4: Chain of energy deposition processes in crystals

Alternatively they cool down by coupling to the lattice vibrations until they reach the top of the valence band (hole) or the bottom of the conduction band (electron). They can also form loosely bound structures called exciton, with an energy slightly smaller than the bandgap energy. The scintillator itself must contain luminescent centers, either intrinsic or extrinsic (doping ions). These molecular systems in the lattice present characteristic transitions between excited states. Recombination brings the release of optical photons, at characteristic wavelength.

2.3.1 Creation of electron hole pairs

To analyze more in depth the mechanisms of the scintillation, we can consider an intermediate energy gamma ray (~ 500 KeV) interacting with the scintillator ma-

terial. In this case the photoelectric effect is dominant. Thus it will produce a hole in a inner shell (usually K shell) and a free or quasifree electron.

$$A + h\nu \rightarrow A^+ + e \quad (2.9)$$

The energy of the primary electron will be $h\nu - E_k$ where E_k is the K level energy. The relaxation then happens differently for electrons and holes.

The ionized atom (A^+) can relax either radiatively, thus emitting a photon, or nonradiatively, generating a secondary electron. This is know as the Auger effect. Thereafter a cascade of both radiative and nonradiative processes takes place. The Auger electron and the primary electron begin a proces of electron-electron scattering or phonon emission. In the case of a radiative emission, the soft x-ray photon emitted may be absorbed producing a new deep hole and free electron.

The electron on the other hand will ionize an atom

$$A + e \rightarrow A^+ + 2e \quad (2.10)$$

The two undistiguishable electrons will undergo a number of other ionization processes, resulting in an avalanche of secondary electrons and holes. At some point the secondary products of these processes are not able to ionize the medium anymore. A fast electron can in principle interact also with valence electrons of the medium, producing collective oscillations known as plasmons. Plasmons behave as quasiparticles, with an energy of ~ 10 eV and can decay into e-h pairs.

This ensemble of avalanche processes continues until the generated secondaries are not able to create further ionization. At this point electrons and holes start to interact with the vibrations of the lattice in a stage called thermalization, via different mechanisms of electron-phonon interaction. As a consequence, at the end of this chain of de-excitation processes, low energy electronic excitations are present: electrons in the conduction band, holes in the valence band, valence excitons, core excitons.

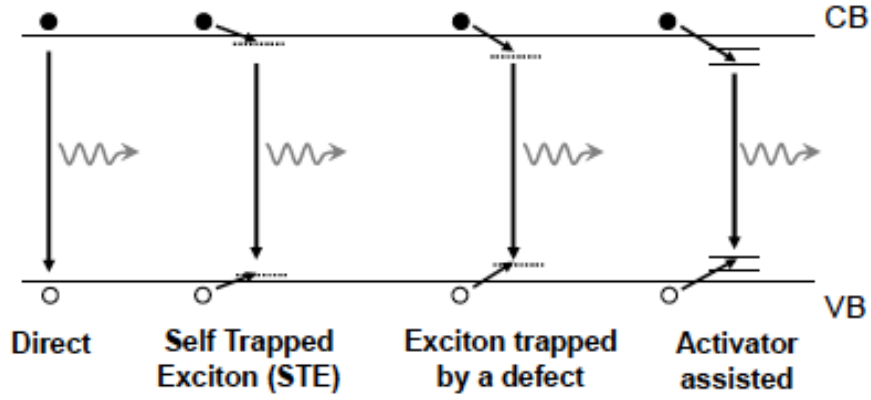


FIGURE 2.5: Different processes for electron hole recombination

2.3.2 Intrinsic luminescence

Electron and holes have several ways to recombine after thermalization and give rise to scintillation photons. The simplest emission process is direct recombination

$$e + h \rightarrow h\nu \quad (2.11)$$

Recombination can more effectively take place when the energy of the electron and hole has decreased, so that they form an exciton. However the various impurities and lattice defects play a very important role in the scintillation process. Thermalized carriers can be bound in some places of the lattice where atom or defects are localized. For example many ionic crystals shows phenomena of localization of the valence hole in the lattice, known as self-trapping. This structure appears when a thermalized hole localizes an anion, polarizing the environment. As a result the hole can be shared between two neighbouring ions forming a V_k center, and the hole is defined as self-trapped hole. For high energy excitation direct creation of valence exciton is unlikely, so V_k centers usually capture free electrons. From subsequent de excitation they can emit photons, thus giving rise to the excitonic luminescence.

$$e + h \rightarrow ex \rightarrow h\nu \quad (2.12)$$

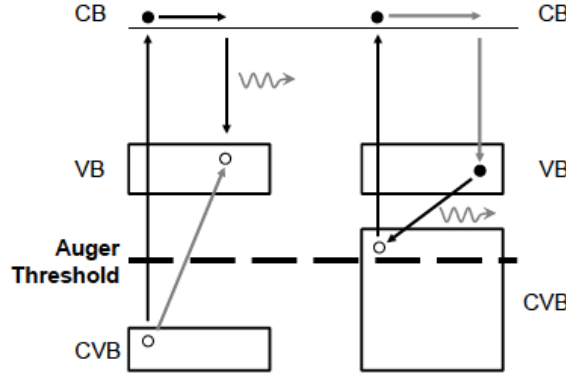


FIGURE 2.6: Direct luminescence (left) versus cross to valence luminescence (right)

2.3.3 Core to valence transitions

If the core bands of the scintillator lie below the Auger threshold, the most favoured transitions involve holes in the valence band and electron in the conduction band. Some systems though present the so-called cross luminescence. This phenomenon implies a direct core to valence transition, due to the fact that holes in uppermost core bands can not deexcite non radiatively(16).

A notable example of core to valence transition is BaF_2 . In this system a Ba^{2+} $5p$ core hole is above the Auger threshold and hence Auger effect does not occur. They can recombine directly with electrons from the valence band, in most of the cases radiatively. This leads to a very fast luminescence given by recombination of the core hole, while the primary electron de excitation is more complex thus leading to a slower component.

2.3.4 Extrinsic luminescence

Most of the scintillator samples used in this work are extrinsic, that is doped with activation centers that can enhance the intrinsic scintillation properties presented above by favouring direct recombination. Rare earth ions doping, for example, is largely used in scintillator technology because of the parity and spin-allowed tran-

sition $4fn - 15d \rightarrow 4fn$. Extrinsic scintillators usually present different luminescent mechanisms driven by activated sites(16):

- $e + h + A \rightarrow ex + A \rightarrow A^* \rightarrow A + h\nu$
- $e + h + A \rightarrow A^{1+} + e \rightarrow A^* \rightarrow A + h\nu$
- $e + h + A \rightarrow (A^{1-})^* + h \rightarrow A + h\nu$
- $A \rightarrow A^* \rightarrow A + h\nu$

In the first case the insertion of dopants is able to sufficiently quench the exciton luminescence so that excitation of radiative centers results from a transfer from excited matrix states. A competing process is the direct capture of free thermalized carriers by luminescent center, in the case of electrons or holes. In heavy doped or self-activated crystals (CeF_3) direct excitation by ionizing radiation is possible.

2.3.5 Quenching phenomena

2.4 Operational parameters

2.4.1 Light yield

One of the feature commonly required of a scintillator is to be have a high light yield, that is to be an efficient converter of radiation to visible light. In this case the relative light output of the scintillator, L_R , can be considered the significant quantity. It is defined as the number of emitted photons per unit of absorbed energy(20)

$$L_R = \frac{N_{ph}}{E_\gamma} \quad (2.13)$$

The number of produced e-h pairs N_{eh} depends on the average energy needed for the creation of a low energy e-h pair, χ_{eh} . This value depends on the type of lattice and band gap of the material, with a numerical coefficient β

$$\chi_{eh} = \beta \cdot g \quad (2.14)$$

If α is the average number of scintillation photons produced by a single e-h pair, the light output is

$$L_r = \frac{\alpha \cdot N_{eh}}{E_\gamma} = \frac{\alpha}{\chi_{eh}} = \frac{\alpha}{\beta \cdot g} \quad (2.15)$$

The coefficient α depends on the transport efficiency of the e-h pairs to the luminescence center and the conversion efficiency of the center itself.

2.4.2 Optical properties and light transport

2.4.3 Rayleigh scattering

Rayleigh scattering is the (dominantly) elastic scattering of light or other electromagnetic radiation by particles much smaller than the wavelength of the light. Rayleigh scattering results from the electric polarizability of the particles. The oscillating electric field of a light wave acts on the charges within a particle, causing them to move at the same frequency. The particle therefore becomes a small radiating dipole whose radiation we see as scattered light. Moreover it is clear that the emission band of a scintillator should lie in the spectral range of the optical transmission of the crystal.

2.4.4 Energy resolution and nonproportionality

In the case of gamma spectroscopy it is necessary to discriminate quanta with different energy. For scintillation detector this fundamental property is characterized by the energy resolution R , defined as Δ/E (in %) where ΔE is the full width at half maximum (FWHM) at pulse height E . It depends on the characteristics of the scintillator, i.e. materials, size and defects as well as the coupling with the photo detector and the parameters of the photo detectors itself. Statistical fluctuations at any step of the detector chain, from dynode multiplication to photo cathode efficiency in the case of a PMT can worsen the resolution at the peak. Thus energy

resolution can be defined as(20)

$$R^2 = R_S^2 + R_{PM}^2 = R_S^2 + \frac{\delta}{E_\gamma} \quad (2.16)$$

where R_S and R_{PM} are, respectively, the scintillator and photomultiplier contributions and δ includes photo electron statistics. It is possible to further decompose the scintillator resolution R_S to take into account the factors depending on the type of scintillator used. In particular it is useful to introduce a term for the transfer efficiency of the optical photons R_t , a term for inhomogeneity R_i and a term for nonproportionality R_n

$$R_S^2 = R_t^2 + R_i^2 + R_n^2 \quad (2.17)$$

The interest lies in the fact that the two terms, for inhomogeneity and nonproportionality, account for the intrinsic resolution of the crystal. Inhomogeneity arise from possible imperfections of the scintillator, such as local variations in the concentration of the dopant or optical defects.

Non proportionality arise when scintillators show deviation from stability of excitation spectrum, that is when linearity between energy of the excitation and relative light output is not preserved. This is particularly important for low energy excitation, since scintillation phenomena occur mainly on the surface. Non proportionality is a cause of the statistical nature of the creation of secondary electrons and photons and contribute to worsen the resolution.

2.4.5 Cerenkov effect

Cerenkov radiation brings important information both in high energy physics and time resolved PET. Cerenkov radiation occurs when a charged particle passes through a dielectric medium at a speed greater than the phase velocity of light in that medium. The phase velocity of light in a medium of refractive index $n > 1$ is

$$v_p = \frac{c}{n} \quad (2.18)$$

A charged particle can travel faster than the speed of light if, given its velocity v_p

$$\frac{c}{n} < v_p < c \quad (2.19)$$

This translates to the following condition for the β coefficient of the particle

$$\beta = \frac{v_p}{c} > \frac{1}{n} \quad (2.20)$$

For a particle of a given mass thus the energy threshold is

$$K_{thr} = mc^2 \left(\frac{\sqrt{n^2 - 1}}{n} - 1 \right) \quad (2.21)$$

The phenomenology of Cerenkov effect can be explained considering the polarization of the medium caused by a charged particle trasversing it. Below the Cerenkov threshold the dipoles sorrounding are simmetrically arranged around the path. As the particle crosses the threshold it travels faster the the speed at which it interacts with the dipoles. This simmetry breaking leads to a non-vanishing dipole moment and thus to the formation of a wave front.

Cerenkov photons are emitted at a characteristic angle in the forward direction, obtained via simple geometrical considerations. The distance traveled by the charged particle in a time t is $t \cdot \beta \cdot c$ whereas the distance along which the photon propagates

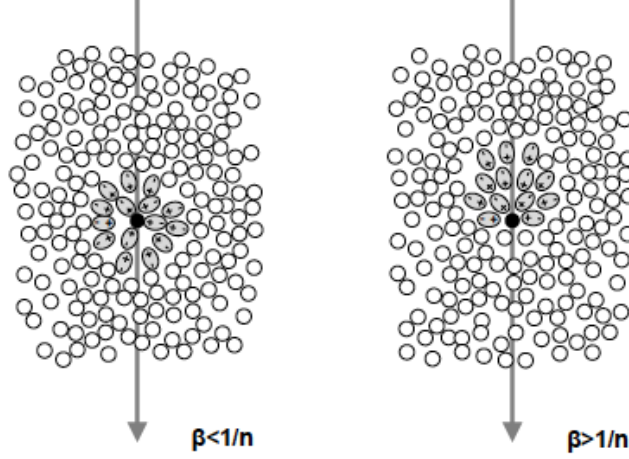


FIGURE 2.7: Phenomenology of Cerenkov effect

is $t \cdot c/n$ as shown in fig. Therefore the characteristic angle at which photons are emitted can be calculated as

$$\cos(\theta_C) = \frac{tc/n}{t\beta c} = \frac{1}{n\beta} \quad (2.22)$$

As will be shown in the next chapter, the direction of emission retains a primary interest in the field of particle identification, while it has a little but non completely negligible impact on timing measurement in PET scanners. It is worth to be noted though that the Cerenkov photons are emitted promptly, taking a relevant share of the first incoming photons. It is useful to consider the number of emitted photons per unit length by a charged particle in function of the wavelength

$$\frac{dN}{d\lambda dx} = \frac{2\pi z^2 \alpha}{\lambda^2} \left(1 - \frac{1}{\beta^2 n^2(\lambda)} \right) \quad (2.23)$$

Neglecting dispersion in the medium, and integrating over an appropriate interval of waveleghts we obtain that the photons are emitted mostly in the UV range.

$$\frac{dN}{dx} = 2\pi z^2 \alpha \left(1 - \frac{1}{\beta^2 n^2(\lambda)} \right) \int_{\lambda_1}^{\lambda_2} \frac{d\lambda}{\lambda^2} = 2\pi z^2 \alpha \sin^2 \theta_C \left(\frac{1}{\lambda_1} - \frac{1}{\lambda_2} \right) \quad (2.24)$$

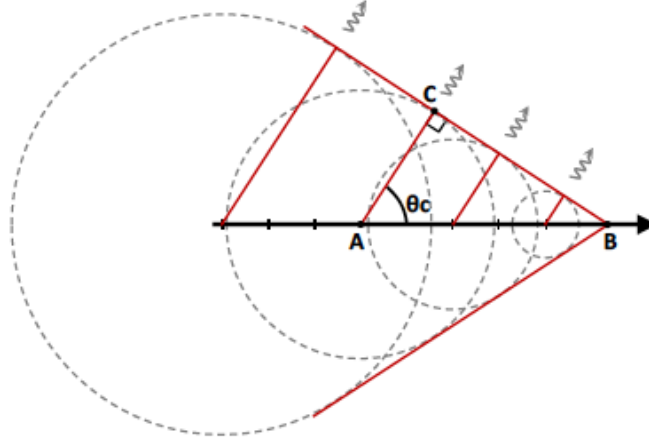


FIGURE 2.8: Sketch of the Cerenkvo emission cone

A simple calculation shows that, even at the low energies that characterize a PET exam (511 KeV), a non negligible number of Cerenkov photons is produced. As an example, it is interesting to consider the case of the most popular crystal for PET detectors, $\text{Lu}_2\text{SiO}_5:\text{Ce}$ (LSO) ($\rho_{\text{LSO}} = 7.48 \text{ g/cm}^3$). Taken a constant value for refractive index (1.82(13)) and given the K-shell binding energy of the electron (63 KeV(24)), we can estimate, with the help of 2.21, the energy threshold for Cerenkov production for electrons at 100 KeV. If we then consider a freed electron from the K-shell and its average range in LSO ($265 \mu\text{m}$ (4)), we can make use of formula 2.24, given that

$$\sin^2(\theta_c) = 1 - \frac{1}{n^2\beta^2} = 0.58 \quad (2.25)$$

The number of optical photons produced in the wavelength range 180 - 800 nm is ~ 40 .

2.5 Scintillators in PET detectors

3

Photo detectors

After the scintillation phase in the crystal, visible photons are generated and coupled to a photodetector. At this stage the photodetector generates an electric signal related to the photon rate, by generating free electrons in vacuum or electron-hole pairs in a semiconductor.

As they are used as fundamental components of the experimental apparatus the vacuum photodetector technology and the solid state technology will be presented. Vacuum photodetectors are characterized by the production of free electrons in an external photocathode by photoelectric interaction. The produced electrons undergo acceleration in a focused electric field and are multiplied by secondary interaction before being transferred to the read out circuitry. Photo multiplier tubes (PMT) and micro channel plates (MCP) are prominent examples of vacuum technology.

In the case of solid state photo detectors, photons interact directly in the bulk material, where electron-hole pairs are produced. The pairs are then accelerated in the electric field and multiplied by ionization in the semiconductor itself. In the work presented here, Silicon photo multipliers (SiPM) are used as representative of this kind of detector.

3.1 Photo multiplier tubes

Photo multiplier tubes are largely used vacuum photo detection devices and have been diffusively discussed in literature(15). In figure 3.1 the main elements of a

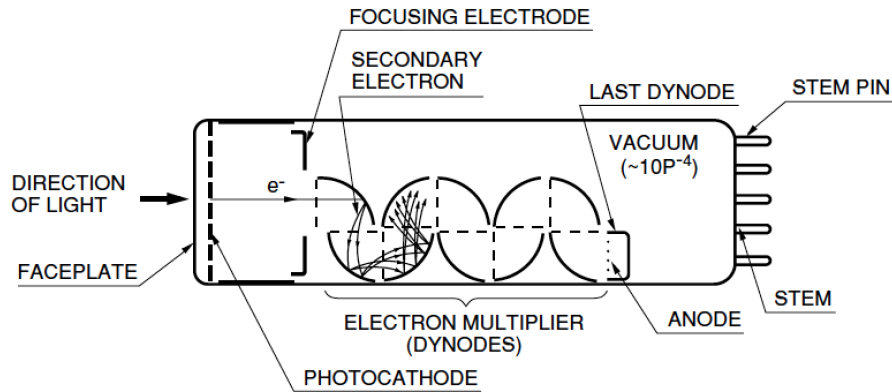


FIGURE 3.1: Schematics of a Photo-Multiplier Tube

photo multiplier tube are sketched:

- a photocathode, which converts visible photons into an electron flux
- an electron-optical input system which focuses and accelerates the electron flux
- an electron multiplier consisting of a series of secondary emission electrodes (dynodes)
- an anode, which collects the electron flux and supplies the output signal

Photoemission is due to a fraction of the incident visible photons that transfer enough energy to the electrons of the photo cathode to extract them. Then the focusing system allows the freed electrons to reach the first dynode, i.e. the first multiplication stage. The electrons are accelerated and focused by electric field between the dynodes and the required potential gradient is usually guaranteed by a voltage divider.

3.1.1 Properties of PMT

- **quantum efficiency:** photocathode are usually made of deposited photo emissive semiconductor. They can be semi transparent or opaque, depending on the place where the emissive material is deposited with respect to the input window. The most used materials are silver-oxygen-caesium ($AgOCs$), antimonyum caesium ($SbCs$), and the bi-and trialkali compounds $SbKCs$, $SbRbCs$, and $SbNa_2KCs$. The most important parameter to be considered is the cathode radiant sensitivity, defined as the ratio of the cathode current I_p to the incident flux Φ

$$S_k(A/W) = \frac{I_p(A)}{\Phi_e(W)} \quad (3.1)$$

The incoming photons have usually a certain spectral composition and the cathode is not uniformly sensitive in this range. With this respect the most used quantity is the quantum efficiency, that is the ratio of the number of photo electrons emitted, n_k , to the number of incident photons, n_i

$$QE = \frac{n_k}{n_i} = S_{k,\lambda} \frac{h \nu}{e} \quad (3.2)$$

where $S_{k,\lambda}$ is the monochromatic sensitivity, defined as

$$S_{k,\lambda} = \lim_{d\lambda \rightarrow 0} \frac{dI_p}{d\Phi_e} \quad (3.3)$$

- **gain:** if the number of photo electrons that reach the first dynode is n , and the gain of the dynode is g_1 , the number of secondary electrons is $n \cdot g_1$. If g_i is the gain of the single dynodes, after N stage the number of electrons collected at the anode are

$$n_a = n \prod_{i=1}^N g_i \quad (3.4)$$

It is possible to define the gain of the photo multiplier as the ratio I_a/I_p where I_a is the anode current given by a photo current I_p . If we define a collection efficiency for each dynode, depending of geometrical parameters, η_i , then the gain G is

$$G = \eta \prod_{i=1}^N \delta_i \eta_i = \eta \prod_{i=1}^N g_i \quad (3.5)$$

- **transit time spread:** transit time spread is the transit-time fluctuation of the signal when identical light pulses hit the same part of the photo cathode. The time resolution of a tube is then often quoted as the FWHM of the probability distribution of the fluctuations. If the probability distribution of electrons arriving at the anode is assumed to be gaussian, then the response $R_\delta(t)$ to a delta-function light pulse is

$$R_\delta(t) = \frac{1}{\sigma_R \sqrt{2\pi}} \exp\left(-\frac{(t - t_{ts})^2}{2\sigma_R^2}\right) \quad (3.6)$$

where t_{ts} is the mean transit time.

3.2 Micro Channel Plate-PMT

A micro channel plate is a two-dimensional array of glass capillaries mounted in parallel as shown in fig 3.2. The diameter of the channels lies in a range of 5 to 20 microns and their internal walls are treated so to have a defined electrical resistance and secondary emissive properties. At both ends of the plate high voltage is applied, so that a primary electron impinging on the wall of a channel produces a multiplication chain. Since they resemble in function a structure of dynode, microchannel plates are usually used in combination with vacuum detector technology in an assembly known as MCP-PMT. An MCP-PMT consists of an entry window, a photo cathode one or more micro channel plates and a collecting anode. To operate and

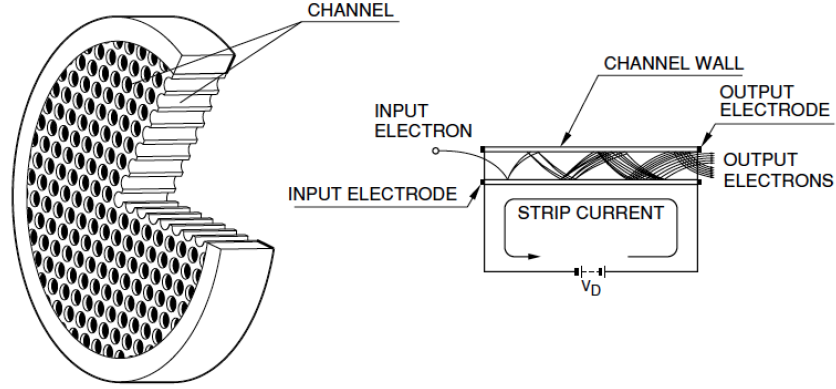


FIGURE 3.2: Work principle of a Micro Channel Plate

MCP it is necessary to provide a certain voltage to the system. To this purpose standard voltage divider circuits are usually adopted, in order to guarantee mostly drifting spaces for electrons before and after the photocathode and multiplication in the MCP stack(11).

3.2.1 Properties of MCP

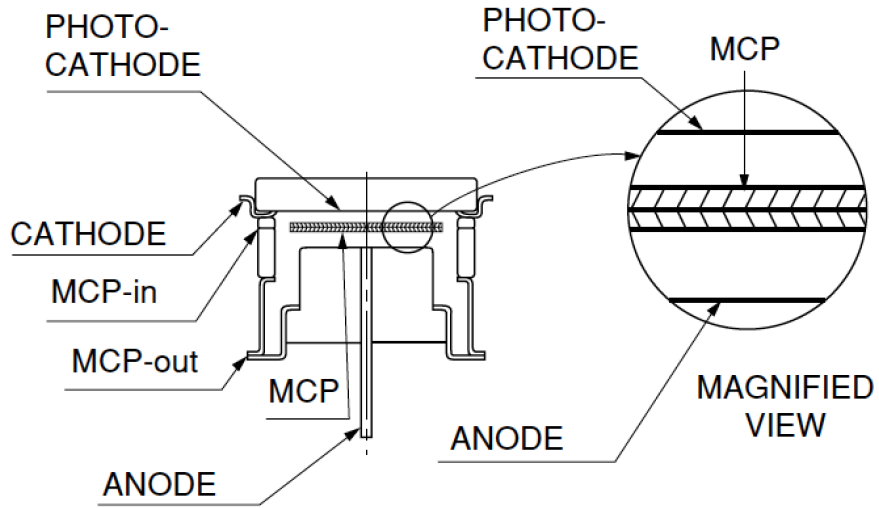


FIGURE 3.3: Schematics of a MCP-PMT

- **quantum efficiency:** in terms of quantum efficiency they do not differ from

standard PMTs, since they make use of the same technology in terms of photo cathodes.

- **gain** The gain of an MCP-PMT depends primarily on the number of plates stacked. Geometrically is determined by the length-to-diameter ratio of a channel α , as

$$G = \exp \left(\frac{\Delta \cdot L}{d} \right) = \exp (\Delta \cdot \alpha) \quad (3.7)$$

where Δ is the gain factor and depends on the plate material, L and d are, respectively, the length and diameter of the micro tube.

- **ion feedback, electron backscattering:** strongly correlated with the characteristics of gain are the problems of ion-feedback and electron backscattering. As the voltage, and thus the gain, increases, it is more and more likely for a photoelectron to be backscattered towards the photo cathode or for an ion to undergo the same process from the stack. Ions can be commonly stripped from residual gas in the drifting area or from interaction in the plate. This leads to the production of secondary pulses, that contribute in the worsen of the time response of the device. Connected to this is also the issue of ageing, since ion bombardment damages the photocathode and it is more and more likely as the vacuum in the device degrades with time. Partial solution to this problem has been found by depositing an Aluminum protection layer on the plate and by modifying the inclination of the micro tubes in the so called Chevron geometry(25).
- **time characteristics:** the rise and fall time of a MCP-PMT are ultra-short, due to the multiplication characteristics of the device. This translated into typical signal contained in a few nanoseconds, or even less. For timing application though the most important parameter to consider is the transit time

spread (TTS). The TTS is the spread in the arrival time of a bunch of photon produced by a converted electron in the photocathode. The time response of MCP-PMTs will be analyzed further in the next chapters.

3.3 Silicon photo multipliers

Recently solid state photo detectors have become competitive with vacuum devices, and for some applications they represent the ideal solution. Their advantage lies in the high photon detection efficiency, their low sensitivity to high magnetic fields, their compactness and cost efficiency(6). In particular the insensitivity to high magnetic fields, given by the feature that no electrons are travelling in the vacuum between dynode and dynode, makes the solid photo detector the first choice for PET-MRI scanners or high energy experiments. With respect to the MCP-PMT, also characterized by high operability in magnetic fields, silicon devices still maintain a high photon detection efficiency, that is the conversion efficiency of incoming photons in to electron hole pairs determining in principle a better energy and time resolution.

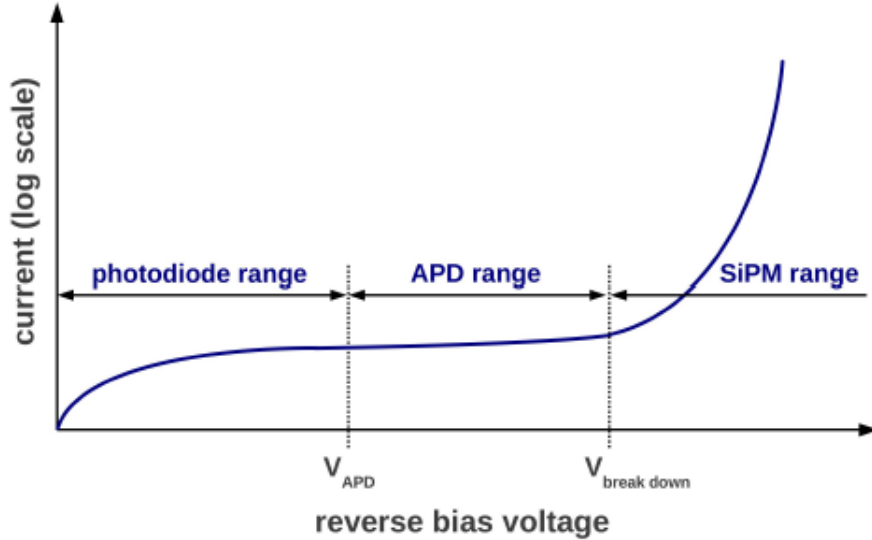


FIGURE 3.4: Voltage current plot for Silicon devices. SiPMs work in Geiger mode.

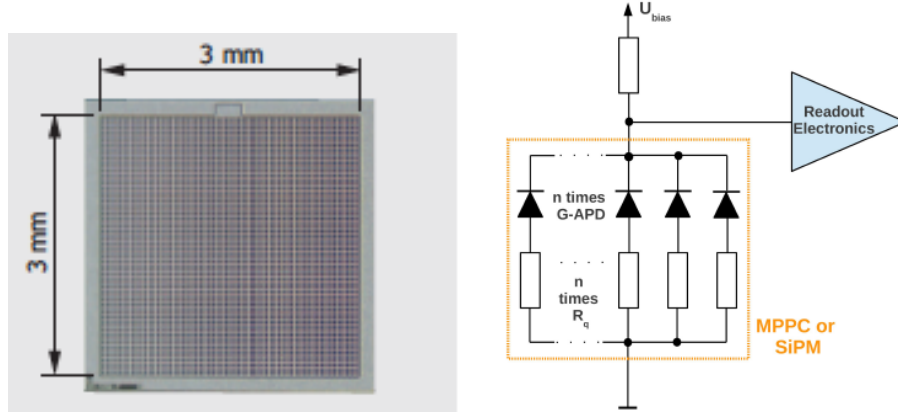


FIGURE 3.5: Example of Hamamatsu MPPC (left) and basic structure of a SiPM (right)

Solid state photo detectors are usually p-n junctions biased reversely and depending on the value of the bias voltage different operational parameters adapt to fundamentally three modes. As seen in figure 3.4 the voltage can applied can be low, as in photo diodes, leading to low currents proportional to the incoming flux. Moving towards the proportionality region the freed electrons are able to ionize further, thus determining a net gain of the device. Avalanche photodiodes (APDs) are a common device operated in this region. Finally a third region, characterized by non-proportionality is the precious operating segment of Geiger mode APD (G-APD). In the Geiger mode region both electrons and holes are able to further ionize the bulk, and the device is sensible to single photo electrons. The created avalanche must be quenched either externally by a series of quenching resistors or actively. Many G-APD cells connected in parallel are the basic structure of silicon photo-multipliers (SiPM) or multi pixel photon counters (MPPC).

3.3.1 Analog SiPM

The structure of an analog SiPM is composed by series of Geiger mode cells in parallel, and the self sustained avalanche is usually quenched by external resistors or active quenching circuitry. The basic schema of a standard SiPM with quenching

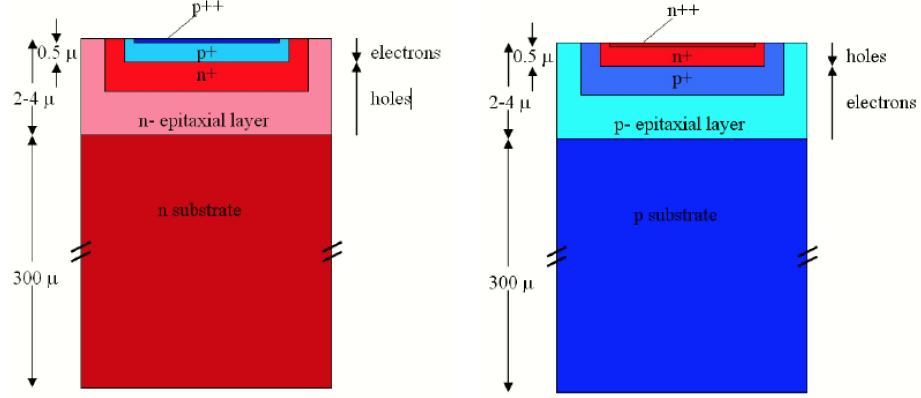


FIGURE 3.6: Layered structure of a IR (left) and UV (right) SiPM

resistors is shown in figure 3.5.

The structure of a G-APD optimized for detection of blue light is shown in figure 3.6. On top of the low resistivity bulk layer an epitaxial layer with a high dopant concentration region is located. The implantation of opposite charge constitutes the p-n junction with a very thin layer extremely doped to assure electric field uniformity. The cell and the quenching resistor are connected on the top surface. Finally a passivation layer (SiO₂) protects the device. Due to its low index of refraction (1.55 in the blue) with respect to the one of Silicon (3.5) Fresnel losses can occur, usually compensated by the presence of anti-reflection coatings.

3.3.2 Properties of SiPM

- **photon detection efficiency:** the photon detection efficiency can be defined as

$$PDE = QE \cdot \epsilon \cdot P_{avalanche} \quad (3.8)$$

where QE is the quantum efficiency, ϵ is the geometric fill factor and $P_{avalanche}$ is the probability of triggering an avalanche. The QE has already been introduced for ordinary photo cathodes and it is comprehensive of Fresnel losses. The fill factor ϵ is defined as the ratio of the sensitive area to the total area of the

detector. Finally the $P_{avalanche}$ is the probability of an electron or hole to cause an avalanche and it depends on the bias overvoltage.

- **gain:** the gain of an analog SiPM can be written as

$$G = \frac{C \cdot U_{ov}}{q} \quad (3.9)$$

where C is the cell capacitance, U_{ov} is the bias overvoltage and q is the charge $q = 1.602 \cdot 10^{-19}C$. This value is typically between 10^5 and 10^7 .

- **spurious events** a dark count is the random production of charge carriers in the depleted region which leads to a regular signal. This type of unwanted event is typically uncorrelated, provided the the dark count rate (DCR) is low enough. It strongly depends of temperature, and typical values range between $100kHz$ to few MHz at $25C$. Optical crosstalk on the other hand is determined by the trigger of an avalanche by an optical photon produced in a neighbouring cell. Indeed optical photons produced in avalanches can travel to other cells, causing correlated spurious pulses. These pulses can occur even after a delay of several microseconds, due to the secondary photons generating electron hole pairs. Moreover charge carriers can be trapped in the bulk and released tens to hundreds of nanoseconds later determining afterpulsing.
- **saturation:** if SiPMs are exposed to high photon fluxes, saturation effects may occur. The detector is intrinsically limited by the number of cells: if the number of photons is small compared to the number of cells provided PDE correction, the SiPM signal is proportional to the light signal. In the opposite case, the signal is saturated.

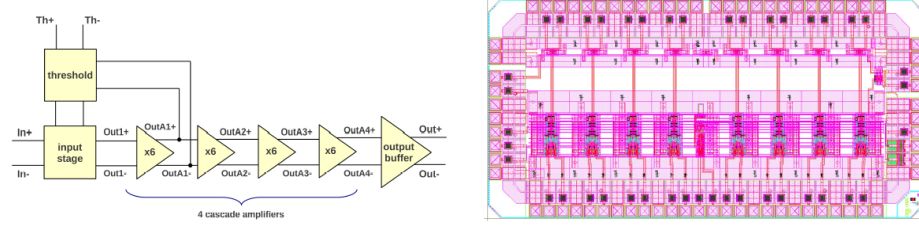


FIGURE 3.7: Structure of the cascade amplifier (left) and scheme (right) of the NINO chip

3.3.3 The NINO chip

Signal generated by SiPMs are in the range of Thus we make use of low noise electronics to read out the detector. In the study presented the ultrafast front-end preamplifier-discriminator chip called NINO, developed at CERN(2). Originally designed for the time-of-flight subdetector of the ALICE experiment, it matches the main requirements of a SiPM readout, that is speed, low noise, minimum slew rate, low input impedance. The chip has eight channels, designed for differential read-out. Each channel is is characterized by an amplifier with 1-ns peaking time, a discriminator with a minimum detection threshold of 10 fC and an output stage.

The input stage is a current-to-voltage converter and the subsequent signal amplification is performed with four identical cascade amplifiers that operate as a discriminator as well. The threshold is set by a voltage difference applied on two symmetrical inputs. The NINO chip makes use of the time-over-threshold technique: a squared output pulse is produced when the leading edge is above the set threshold, encoding the timing information. The width of this signal, on the other hand, is a function of the charge collected, thus encoding the energy information.

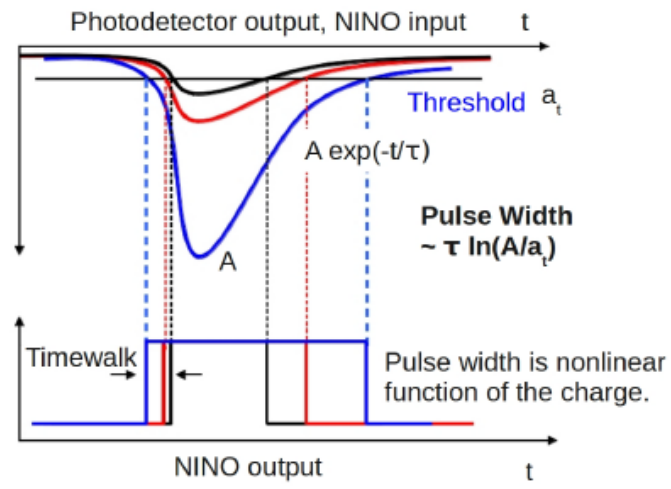


FIGURE 3.8: Principle of operation of a time-over-threshold discriminator

A model for scintillation counting

4.1 Signal formation

4.1.1 *Scintillation pulse*

It is customary to describe (12) the scintillation pulse as a sum of exponentials. The processes introduced in the previous paragraph, focus the attention on the first step of recombination, and the subsequent radiative transitions. All the processes that characterize electron hole relaxation and particularly thermalization of the pairs, lead to oscillations with respect to the start of the scintillation pulse determining a non zero rise time. For all the practical purposes of this work rise time will be modeled by one or more exponential time components τ_r . For what concerns recombination, the radiative transitions can be described by one or more exponential decay times τ_d . In the case of LSO:Ce, for example, the transition takes place between the lowest 5d level, which lies just below the conduction band, and two 4f levels, above the valence band. The parity allowed transition accounts for very fast decay times (*sim* 40 ns).

We can consider, then, the absorption of a γ photon at a time θ . For many scintillators, we can describe the probability density function for the emission times

as the convolution of two exponential functions representing the energy transfer processes and the radiative decay(23):

$$p_t(t|\theta) = \int_{-\infty}^{\infty} \exp\left(-\frac{t'}{\tau_r}\right) \exp\left(-\frac{t-t'}{\tau_d}\right) \theta(t') \theta(t-t') dt' \quad (4.1)$$

In the case different processes contribute to the scintillation pulse via different energy transfer mechanisms, it may be necessary to consider them(22)

$$p_t(t|\theta) = \begin{cases} 0, & t < \theta \\ \sum_i S_i \frac{1}{\tau_{d,i} - \tau_{r,i}} \cdot \left[\exp\left(-\frac{t-\theta}{\tau_{d,i}}\right) - \exp\left(-\frac{t-\theta}{\tau_{r,i}}\right) \right], & t > \theta \end{cases} \quad (4.2)$$

4.1.2 Cerenkov pulse

4.2 The Cramer-Rao lower bound

In general, the emission times t of the detected N photons can be considered statistically independent and identically distributed (iid). Most photo detectors can be modeled as ideal photon counters, able to detect a time stamp for every incoming photon, a set $T_N = \{t_1, t_2, \dots, t_N | \theta\}$.

In order to account for the smearing introduced by the resolution of the detector on the photon time stamps, it is necessary to define its response p_T . In particular it can be modeled by a Gaussian with a variance equal to the single photon time resolution (SPTR) and a mean equal to the transit time t_{TT} . The function is truncated at $t = 0$ not to allow negative transit times.

$$p_T = \frac{1}{\sqrt{2\pi}\sigma_{SPTR}} \exp\left[-\frac{(t - t_{TT})^2}{2(\sigma_{SPTR})^2}\right] \quad (4.3)$$

The corresponding pdf for the time stamps is then a convolution of the photon emission rate and the smearing of the detector.

$$p_{t_n}(t|\theta) = p_t(t|\theta) * p_T(t) = \int_{-\infty}^{\infty} p_t(t-x|\theta) \cdot p_T(x) dx = \int_0^{t-\theta} p_t(t-x|\theta) \cdot p_T(x) dx \quad (4.4)$$

And the integral gives

$$p_{t_n}(t|\theta) = A \cdot \sum_i \frac{S_i}{\tau_{d,i} - \tau_{r,i}} \cdot [a_{\tau_{d,i}}(t|\theta) - a_{\tau_{r,i}}(t|\theta)] \quad (4.5)$$

where

$$a_\tau(t|\theta) = \frac{1}{2} \exp\left(\frac{\sigma_{SPT}^2 - 2t\tau + 2\theta\tau + 2t_{TT}\tau}{2\tau^2}\right) \quad (4.6)$$

$$\cdot \left[\operatorname{erf}\left(\frac{t - \theta - t_{TT} - \frac{\sigma_{SPT}^2}{\tau}}{\sigma_{SPT}\sqrt{2}}\right) + \operatorname{erf}\left(\frac{t_{TT} + \frac{\sigma_{SPT}^2}{\tau}}{\sigma_{SPT}\sqrt{2}}\right) \right] \quad (4.7)$$

The Fisher Information $I(\theta)$ is defined as

$$I(\theta) = \int_{-\infty}^{\infty} \left[\frac{\partial}{\partial \theta} \ln p_{t_n}(t|\theta) \right]^2 p_{t_n}(t|\theta) dt \quad (4.8)$$

Since the samples are iid, the information is additive, so that

$$I(\theta) = N \cdot \int_{-\infty}^{\infty} \left[\frac{\partial}{\partial \theta} p_{t_n}(t|\theta) \right]^2 \frac{1}{p_{t_n}(t|\theta)} dt \quad (4.9)$$

The Cramer Rao theorem states that the variance of any unbiased estimator $\hat{\theta}$ of θ is bounded by the reciprocal of the Fisher information:

$$\operatorname{var}(\hat{\theta}) \geq \frac{1}{I(\theta)} \quad (4.10)$$

In a PET-like experiment the interest lies in the estimate of the photon time of interaction θ . Statistically speaking the Cramer Rao theorem gives the intrinsic time resolution limit for any given scintillator with the given parameters.

4.3 The order statistics

If it is assumed a specific order in the set of recorder timestamps, it is evident that they are neither independent nor identically distributed. By sorting the elements in

T_N we can create an ordered set $T_{\bar{N}} = \{t_{\bar{1}} \leq t_{\bar{2}} \leq \dots \leq t_{\bar{N}}\}$. The pdf for the n th-order statistics is given by(22)

$$f_n|N(t\theta) = \binom{N}{n} \cdot n \cdot P_{t_n}^{n-1}(t|\theta) \cdot [1 - P_{t_n}(t|\theta)]^{N-n} \cdot p_{t_n}(t|\theta) \quad (4.11)$$

In this case the set is not iid; thus considering an estimator using a unique timestamps, as the case of analog SiPMs, the Fisher information is

$$I_n(\theta) = \int_{-\infty}^{\infty} \left[\frac{\partial}{\partial \theta} \ln f_n(t|\theta) \right]^2 f_n(t|\theta) dt \quad (4.12)$$

4.4 Intrinsic time resolution

4.5 Effects on signal extraction

MonteCarlo simulation tools

5.1 Ray tracing

5.2 Geant4

5.2.1 Physics

5.2.2 Implementation

5.3 SLitrani

5.3.1 Physics

5.3.2 Implementation

5.4 A comparison for timing simulation

5.5 Simulation input parameters

5.5.1 Light yield

The measured light output depends on the absolute yield of the crystal as well as on instrumental and physical factors

- the temperature dependence of the scintillator output
- the reflectivity of the wrapping material

- the condition of the crystal faces
- the relation between the refractive index of the crystal and the photo detector
- the quantum efficiency of the photo detector
- the collection efficiency of the charges produced in the photo detector

To measure the light output of sample crystals the number of photo electrons N_{pe} collected can be used. The number of photo electrons can be calculated by comparison with the position of the photo electric peak with respect to the signal produced by a single photon. The number of photo electron per MeV of the incident γ particle can be determined as

$$N_{pe}/MeV = \frac{\text{position photo peak}}{\text{position single photo electron peak}} \cdot \frac{A_1}{A_2} \cdot \frac{1}{E_\gamma} \quad (5.1)$$

where E_γ is the energy of the incident γ particle and linearity of the detector response is assumed. A pedestal may be subtracted from the position of the peaks. A_1 and A_2 are the values of the attenuation of the signal in the case of the photo peak and the single electron peak, i.e.

$$A_i = e^{\frac{B_i}{20}} \quad (5.2)$$

and B_i is the attenuation in dB.

The number of photons emitted per MeV can be determined if the quantum efficiency of the photo detector is known:

$$N_{ph}/MeV = \frac{N_{pe}}{q_{eff}} \quad (5.3)$$

The position of the photo peak and the resolution on the peak are determined with a fit. The fitting function is the sum of a Gaussian and a Fermi distribution:

$$y(x) = \frac{P}{e^{\frac{x-C}{R}} + 1} + Ae^{-\frac{(x-\mu)^2}{2\sigma^2}} \quad (5.4)$$

where P, C and 1/R correspond to height, position and slope of the Compton edge, A is the height of the photo peak with position μ and FWHM width 2.35σ . An example of the spectrum fitted with $y(x)$ is shown in figure.

The measurements were performed placing the crystal on top of a *Photonis XP2020Q* photo multiplier tube with the following characteristics:

- Bi-Alkali photo cathode
- Refraction index 1.48 (at 420 nm)
- Peak sensitivity at 420 nm

The absorption spectra of the photo cathode is shown in figure. The quantum efficiency of the PMT was measured experimentally with the following the set up: a light source was sent into a monochromator, the beam was then split in two, and both the PMT to measure and a calibrated photo diode are enlightened. The process was repeated for every wavelength between 250 and 700 nm. The results obtained assessed a quantum efficiency of 0.22 in the UV.

The light output has been measured stimulating scintillation by γ rays from a ^{137}Cs source ($E_{\text{gamma}} = 662 \text{ keV}$) with an activity of $\sim 200 \text{ kBq}$ placed a few mm above the crystal. The system crystal-PMT was placed inside a black box, with controlled temperature (20°C) to avoid drift in the system response. Further shielding against background light was ensured by an aluminum cap covering the entry window of the PMT. After the collection of the photo electrons at the anode of the PMT, the signal is attenuated, shaped and stored by the DAQ, with a digitizer *CAEN DT5720*.

To correct for long-term variations of the PMT gain and quantum efficiency, the measured light yield was normalized to the light yield of a reference crystal with well known light output. The reference crystal used is a $2 \times 2 \times 10 \text{ mm}^3$ LuAP

crystal encapsulated into Teflon to protect it. In order to normalize the light outputs obtained, the number of photo electrons correspondent to the peak for the reference crystal is required. The number of photo electrons has been evaluated given the single electron response of the crystal. The signal produced by a single photo electron and the position of the pedestal were determined by recording the unattenuated PMT signal with the DAQ software: the PMT is covered with a black box and the trigger is lowered to the minimum. The histogram leads to a double peak: one for the electronic noise, one for the single electron. Background noise is due to charge carriers thermally generated in the electronics and electron released in one of the dynodes by γ photons from the source. The number of photo electrons generated per MeV by the $2 \times 2 \times 10 \text{ mm}^3$ LuAP crystal is 1767.

5.5.2 Optical transmission

5.5.3 Fluorescence spectrum

6

Methods

6.1 Time Correlated Single Photon counting

6.1.1 *Excitation*

6.1.2 *Detection*

6.2 Data analysis techniques

6.2.1 *Iterative reconvolution*

In time correlated single photon counting experiments the problem at hand is statistically speaking to estimate or more parameters (the lifetimes) from a dataset.

The maximum likelihood method is considered to be the most powerful method of parameter estimation. Consider n independent observations (counts in this case) c_1, \dots, c_n and a vector of parameters $\theta = (\theta_1, \dots, \theta_m)$. If the probability of having the observation i is $p(c_i|\theta)$, the likelihood function is

$$L(c_1, \dots, c_n|\theta) = \prod_{i=1}^n p(c_i|\theta) \quad (6.1)$$

The Maximum Likelihood method provides then an estimate of the true parameters' value as the vector θ that maximizes the likelihood function. In the case of time

correlated single photon counting it is natural to assume that the observed counts c_i follow a Poisson distribution

$$p(c_i|\theta) = \exp(-\langle c_i \rangle) \frac{\langle c_i \rangle^{c_i}}{c_i!} \quad (6.2)$$

where $\langle c_i \rangle$ is the expected value of the number of counts in the i-channel. This expected value is given by the model taken in to consideration: in this case we can make use of the equations obtained in chapter 3. The pdf for the time stamps is given by

$$p_{t_n}(t|\theta) = A \cdot \sum_i \frac{S_i}{\tau_{d,i} - \tau_{r,i}} \cdot [a_{\tau_{d,i}}(t|\theta) - a_{\tau_{r,i}}(t|\theta)] \quad (6.3)$$

where

$$a_\tau(t|\theta) = \frac{1}{2} \exp\left(\frac{\sigma_{SPTR}^2 - 2t\tau + 2\theta\tau + 2t_{TT}\tau}{2\tau^2}\right) \quad (6.4)$$

$$\cdot \left[\operatorname{erf}\left(\frac{t - \theta - t_{TT} - \frac{\sigma_{SPTR}^2}{\tau}}{\sigma_{SPTR}\sqrt{2}}\right) + \operatorname{erf}\left(\frac{t_{TT} + \frac{\sigma_{SPTR}^2}{\tau}}{\sigma_{SPTR}\sqrt{2}}\right) \right] \quad (6.5)$$

Thus the expected number of counts for the i-channel is

$$\langle c_i \rangle = \int_{(i-1)\Delta}^{i\Delta} p_{t_n}(t|\theta) dt + b_i = g_i(\theta) \quad (6.6)$$

where Δ is the time channel width and b_i accounts for the average number of dark counts in the channel i. The vector of parameters θ is given by the lifetimes τ_i , the relative intensities S_i and a zero time shift δ . It is customary to determine the best estimate for θ by minimizing the function $-\ln(L)$ since the log-likelihood function attains its maximum for the same value as the likelihood function. In the specific case the function to minimize is

$$- \ln(L) = - \prod_{i=1}^n \exp -g_i \frac{g_i^{c_i}}{c_i!} = \sum_{i=1}^n -g_i + c_i \ln(g_i) - \ln(c_i!) \quad (6.7)$$

which is equivalent to minimizing the Poisson deviance(3)

$$f = \sum_{i=1}^n -g_i + c_i \ln(g_i) \quad (6.8)$$

The standard function minimized in standard fluorescence analysis is usually the χ^2 defined as

$$\chi^2 = \sum_{i=1}^n \frac{[c_i - g_i(\theta)]^2}{c_i} \quad (6.9)$$

or, in the modified least square method(3)

$$\chi_m^2 = \sum_{i=1}^n \frac{[c_i - g_i(\theta)]^2}{g_i} \quad (6.10)$$

When the number of counts is large they are numerically very close, since the Poisson distribution can be approximated by the Gaussian. Nevertheless in the data analysis the maximum likelihood estimator will be used, since it is preferable the more the low-count region of the decay influences the estimated parameters(3).

6.2.2 Error estimation

6.3 Simulations

Na-22 measurement

7.1 Phenomenology

The physics of γ photon interaction have been already introduced in chapter 2. In order to build a time correlated single photon counting experiment two time signals are necessary, a start signal and a stop signal. A simple way to obtain this is to use a β^+ active isotope, such as Na^{22} . This isotope emits a positron according to the decay reaction $^{22}Na \rightarrow ^{22}Ne + \beta^+ + \bar{\nu}_e + \gamma$. The positron yield is relatively high, 90.4%, and competitive processes are electron capture (EC) and direct transition to the Ne ground state. In the positron emission case the Ne ground state is reached after 3.7 ps by emission of a γ quantum of 1.274 MeV. The half life of the isotope is 2.6 years. It is worth to note that, as outlined in chapter 2 the Cerenkov threshold for heavy scintillators is below the energy of the annihilation gamma produced by the isotope.

7.2 Experimental setup

The components of the apparatus were placed in a cooled black box. Cooling is necessary to maintain the performance of SiPM

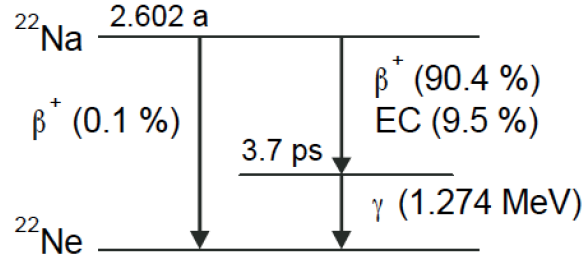


FIGURE 7.1: Decay scheme of Na^{22}

The start signal is obtained by mean of a LSO crystal. The reference crystal is readout by a SiPM board amplified by a NINO chip.

7.3 Preliminaries

7.3.1 Characteristics of the start signal

7.3.2 Characteristics of the stop signal

7.3.3 IRF measurements

7.3.4 Control of the bias fraction

7.4 Data analysis

7.4.1 Cuts

7.4.2 Fit procedure

7.4.3 Results

VUV measurement

8.1 High Harmonic Generation

When an atom is exposed to a strong laser field it can absorb a large number of photons through non linear processes. This energy can be transferred back to the photon field. The phenomenon of high order harmonic generation of a laser field is a nonlinear effect that results in the emission of photons of frequency multiple of the source frequency. For example a rare gas traversed by a sufficiently power laser field may give rise to harmonic generation.

In figure 8.1 the main details of the high harmonic generation process are summarized, in a semi-classical configuration and as a quantum wave process. If the laser field is strong enough ($\sim 10^{10}\text{V/m}$), it can allow the electron to tunnel through the barrier. The electron itself sits unperturbed in the well until the field of the laser sums to the atom potential bending it. The electron gets accelerated in the laser field and it can recollide with the atom itself. The electron kinetic energy is then transferred into photons. The cut-off energy can be calculated by examining the maximum energy the ionized electron can gain in the electric field of the laser,

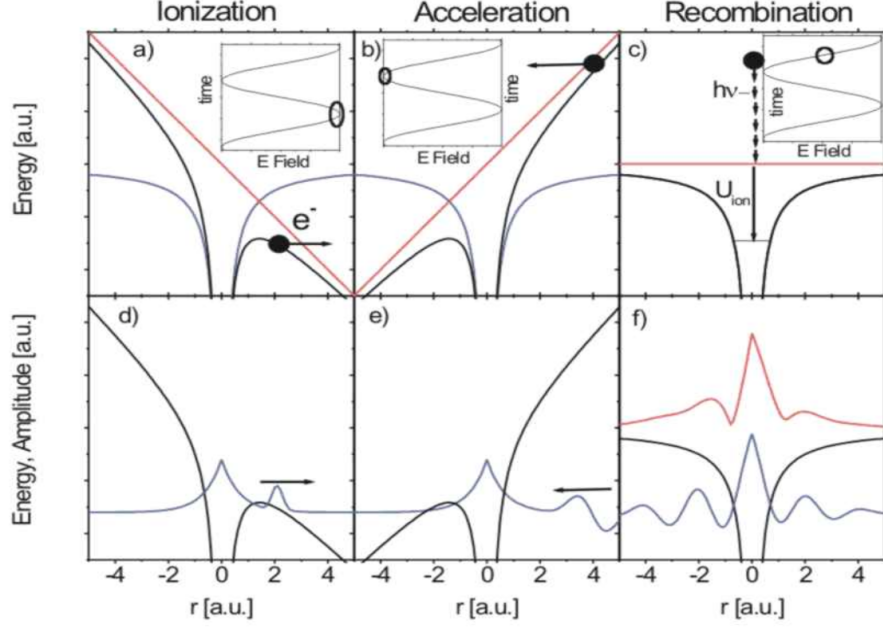


FIGURE 8.1: Phenomenology of High Harmonics Generation

that is

$$E_{max} = I_p + 3.17U_p \quad (8.1)$$

where U_p is the ponderomotive energy from the laser and I_p is the ionisation potential. The recollision leads to the emission of a very broad light spectrum. The ionization and recollision happen on each half cycle of the laser pulse, and the spectra are added coherently. As a consequence the spectrum is structured in odd harmonics. High harmonics constitute a source of soft X-rays that retains the time characteristics of the driving laser, in terms of bunch structure and repetition rate. The harmonic cut off varies with the laser intensity up to saturation. The saturation intensity depends on atomic species of the noble gas used as a medium to produce the harmonics.

8.2 Experimental setup

The setup available at CELIA it is presented in (18). it will be briefly described here. The line is organized in two different room. A first room is devoted to the

laser amplification system, while in the experimental room the high harmonics are produced.

8.2.1 Laser beamline

The AURORE beamline is based on a amplified Ti-sapphire femtosecond oscillator. The Ti-sapphire oscillator generates 30 fs pulses, at 1 nJ and a frequency of 80 MHz. Before amplification the pulses are stretched up to 280 ps for optical power reasons. The regenerative pre amplifier brings the energy of the beam to 700 J at 1 kHz. The beam is then amplified in a Ti:sapphire crystal pumped by four synchronised Nd:YLF lasers at 532 nm and 15 W. At the end of the amplification chain the laser beam delivered has a power of 10 W for 170 ps and it is sent to the experimental room.

8.2.2 VUV line

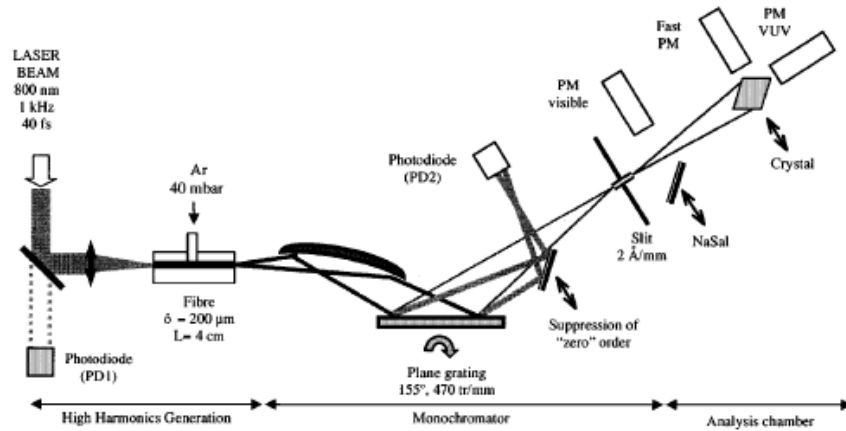


FIGURE 8.2: Schematics of the VUV line at CELIA Bordeaux

Before high harmonic generation the beam is compressed again down to 35 fs, centered around 800 nm at 1 kHz, with an energy of 4 mJ. A schematic of the HH VUV beamline is presented in fig The elements are under vacuum at a pressure of 10^{-6} mbar. The beam is focused in the fiber containing the gas (200m in diameter and

4 cm length). Depending on the gas used and the pressure condition the energy of the harmonic lines and the efficiency of the process may vary. Typically in Argon/Neon the energy of the harmonics is between 10 eV and 120 eV. The fundamental beam and the harmonics spread at the exit of the fiber and are sent to the monochromator where a toroidal mirror and a plane grating (470 lines/mm) focus the selected wavelength on the exit slit. The zero order is suppressed by a plane mirror at an angle tuned on the grating system. The desired VUV-XUV beam selected in energy is then directed to the sample placed in a vacuum chamber. Due to the dispersion by the grating the output pulses are stretched in time, and they have been measured with a VUV-streak camera to be 2-3 ps FWHM.

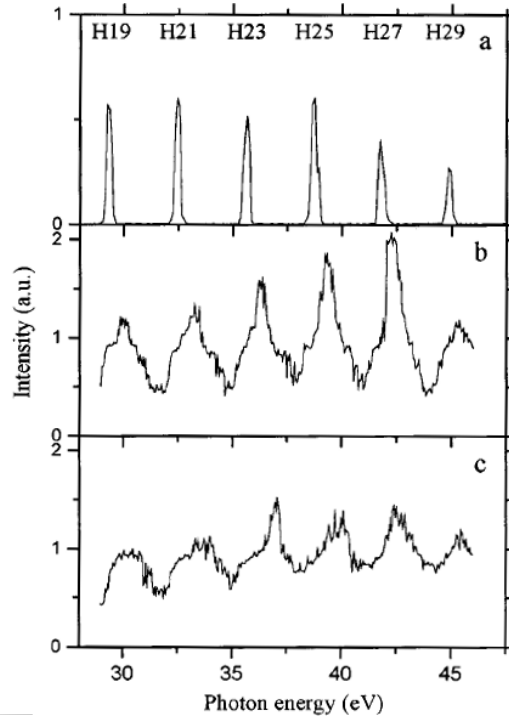


FIGURE 8.3: Schematics of the VUV line at CELIA Bordeaux

8.2.3 Detection system

The light produced by the luminescent sample hit by the VUV-XUV radiation is collected by an optical fibre visible-UV of 0.6 mm diameter mounted on a side of the chamber and connected to a monochromator (TRIAX Jobin-Yvon 130) by a focalisation system. The monochromator is equipped with three diffraction gratings, one with 1200 lines/mm and the others with 300 lines/mm. This allows to cover a spectral range between 200 nm and 1000 nm.

The photon counting device is a Hamamatsu MCP-PMT R3809U-52 model. The DAQ system is shown in figure ???. The signal from the laser trigger is routed into a Ortec Pico Timing Discriminator (model 9307). A first output is directed directly to a Ortec Time to Analog Converter (model 9308). A second output is directed to a Lecroy Quad Coincidence Unit (model 622). The MCP-PMT signal is preamplified by a ORTEC 1-GHz preamplifier (model 9306) with a gain of 100 and then sent to a second Pico Timing Discriminator. One output is sent to the Lecroy Quad Coincidence Unit and a second one delayed by 60 ns and sent to the TAC. The last unit is required since the laser trigger has a fixed delay. A third output is sent to a SR400 Gated Photon Counter (Stanford Research System) along with the output of the Lecroy coincidence unit. The SR400 Gated Photon Counter allows to determine the rate of counts at the MCP detector, to keep under control the fraction of biased events. The TAC guarantees a 16-bit digital resolution in the range 0-325 s down to a binning of 1.22 ps and its signal is sent to a computer for the software system to finally determine the delay between the MCP and the laser trigger.

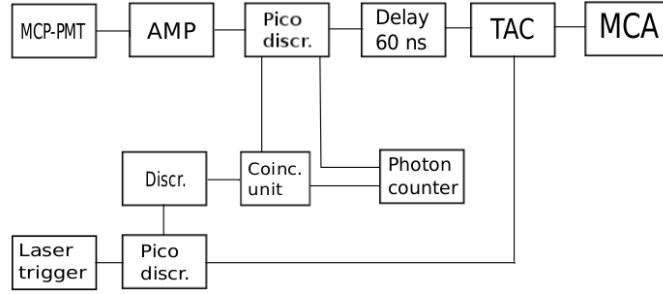


FIGURE 8.4: Schematics of DAQ system

8.3 Preliminaries

8.3.1 *VUV spectrum*

8.3.2 *IRF measurement*

8.3.3 *Control of the bias fraction*

8.4 Data analysis

8.5 Fit procedure

8.6 Results

9

Conclusions

Bibliography

- [1] Braccini Amaldi. Present challenges in hadrontherapy techniques. *The European Physical Journal Plus*, (126):70–85, 2011.
- [2] Jarron et al. Anghinolfi. Nino: An ultrafast low-power front-end amplifier discriminator for the time-of-flight detector in the alice experiment. *IEEE Transactions on Nuclear Science*, 51(5):1974–1978, 2004.
- [3] Therneau et al. Bajzer. Maximum likelihood method for the analysis of time-resolved fluorescence decay curves. *European Biophysics Journal*, 20(5):247–262, 1991.
- [4] Coursey et al. Berger. Stopping-power and range tables for electrons, protons, and helium ions. 2005.
- [5] Shakirin et al. Crespo. Direct time-of-flight for quantitative, real-time in-beam pet: a concept and feasibility study. *Physics in Medicine and Biology*, (52):6795–6811, 2007.
- [6] Filatov et al. Dolgoshein. Silicon photomultiplier and its possible applications. *Nuclear Instruments and Methods in Physics Research A*, 504:48–52, 2003.
- [7] Loeffler Durante. Charged particles in radiation oncology. *Nature Reviews Clinical Oncology*, (7):37–43, 2010.
- [8] Crespo et al. Enghardt. Charged hadron tumour therapy monitoring by means of pet. *Nuclear Instruments Methods in Physics Research A*, (525):284–288, 2004.
- [9] Soerjomataram et al. Ferlay. *Cancer Incidence and Mortality Worldwide: IARC CancerBase No. 11*. International Agency for Research on Cancer, 2012.
- [10] Crespo et al. Fiedler. The feasibility of in-beam pet for therapeutic beams of he. *IEEE Transactions in Nuclear Science*, 53(4):2252–2260, 2006.
- [11] Hamamatsu. *Photomultiplier Tubes - Basic and Applications*. Hamamatsu, 2006.

- [12] Schluter Hyman, Schwarcz. Study of high speed photomultiplier systems. *The Review of Physical Instruments*, 35(3):393–406, 1963.
- [13] Specht et al. Jellison. Spectroscopic refractive indices of monoclinic single crystal and ceramic lutetium oxyorthosilicate from 200 to 850 nm. *Journal of Applied Physics*, 112, 2012.
- [14] Surti et al. Karp. The benefit of time-of-flight in pet imaging: Experimental and clinical results. *Journal of Nuclear Medicine*, 49:462–470, 2008.
- [15] Knoll. *Radiation Detection and Measurement*. Wiley, 2000.
- [16] Annenkov et al. Lecoq. *Inorganic Scintillators for Detector Systems*. Springer, 2006.
- [17] Linz. *Ion Beam Therapy*. Springer, 2012.
- [18] Belsky et al. Martin. Time-resolved studies of scintillation materials with vuv harmonic ultrashort pulses laser source. *IEEE Transactions on Nuclear Science*, 48(4):1137–1143, 2001.
- [19] Parodi. *On the feasibility of dose quantification with in-beam PET data in radiotherapy with C and proton beams*. PhD thesis, Technischen Universitat Dresden, November 2004.
- [20] Rodnyi. *Physical Processes in Inorganic Scintillators*. CRC Press, 1997.
- [21] Steidl et al. Schardt. Precision bragg-curve measurements for light-ion beams in water. *GSI Scientific Report*, 2007.
- [22] van Dam Seifert, Schaart. The lower bound on the timing resolution of scintillation detectors. *Physics in Medicine and Biology*, (57):1797–1814, 2012.
- [23] Shao. A new timing model for calculating the intrinsic timing resolution of a scintillator detector. *Physics in Medicine and Biology*, (52):1103–1117, 2006.
- [24] Attwood et al. Thompson. *X-Ray Data Booklet*. Lawrence Berkeley National Laboratory, University of California, 2009.
- [25] Va’vra. Ion feedback suppression using inclined mcp holes in a single-mcp + micromegas + pads detector. *Proceeding of Nuclear Science Symposium Conference Record*, 2:1142–1146, 2004.
- [26] Wilson. Radiological use of fast protons. *Radiology*, (47):487–491, 1946.